© 2019. Published by The Company of Biologists Ltd | Journal of Cell Science (2019) 132, jcs225383. doi:10.1242/jcs.225383

RESEARCH ARTICLE

Altering integrin engagement regulates membrane localization of $K_{ir}2.1$ channels

Swarnali Sengupta, Katheryn E. Rothenberg, Hanjun Li, Brenton D. Hoffman* and Nenad Bursac*

ABSTRACT

How ion channels localize and distribute on the cell membrane remains incompletely understood. We show that interventions that vary cell adhesion proteins and cell size also affect the membrane current density of inward-rectifier K^+ channels ($K_{ir}2.1$; encoded by *KCNJ2*) and profoundly alter the action potential shape of excitable cells. By using micropatterning to manipulate the localization and size of focal adhesions (FAs) in single HEK293 cells engineered to stably express $K_{ir}2.1$ channels or in neonatal rat cardiomyocytes, we establish a robust linear correlation between FA coverage and the amplitude of $K_{ir}2.1$ current at both the local and whole-cell levels. Confocal microscopy showed that $K_{ir}2.1$ channels accumulate in membrane proximal to FAs. Selective pharmacological inhibition of key mediators of protein trafficking and the spatially dependent alterations in the dynamics of $K_{ir}2.1$ fluorescent recovery after photobleaching revealed that the $K_{ir}2.1$ channels are transported to the cell membrane uniformly, but are preferentially internalized by endocytosis at sites that are distal from FAs. Based on these results, we propose adhesion-regulated membrane localization of ion channels as a fundamental mechanism of controlling cellular electrophysiology via mechanochemical signals, independent of the direct ion channel mechanogating.

KEY WORDS: Cardiac potassium channel, Endocytosis, Focal adhesion, Mechanotransduction, Micropatterning

INTRODUCTION

The activity of inwardly rectifying K^+ channels, such as $K_{ir}2.1$ (encoded by *KCNJ2*) (Hibino et al., 2010), sets the resting membrane potential of various excitable cells (e.g. cardiomyocytes, neurons, smooth and skeletal muscle cells) to a highly negative (hyperpolarized) value. During action potential firing, a hyperpolarized membrane potential enables the voltage-gated Na^+ channels (e.g. cardiac sodium channel, $Na_v1.5$, encoded by *SCN5A*) to transiently depolarize the cell membrane to positive potentials, followed by the return to the original resting state. In the heart, the $K_{ir}2.1$-mediated I_{K1} current is upregulated during development (Wahler, 1992; Huynh et al., 1992), but downregulated in certain pathologies. These include myocardial infarction, heart failure (Beuckelmann et al., 1993; Nattel et al., 2007) and Anderson–Tawil syndrome (Bendahhou et al., 2003), a congenital disease characterized by periodic paralysis and polymorphic tachycardias (Miake et al., 2003; Hibino et al., 2010). Such electrophysiological changes in the heart are often associated with profound alterations in cardiomyocyte size and shape, and the extracellular matrix (ECM), as well as cytoskeletal tension (Jacot et al., 2010; Peter et al., 2016). Cardiomyocytes sense physical changes in their environment through integrins (Ross and Borg, 2001), heterodimeric receptors for ECM proteins that relay information to focal adhesions (FAs), force-sensitive subcellular structures connected to actin cytoskeleton (Kanchanawong et al., 2010; Geiger et al., 2009). In different systems, dynamic changes in FA proteins, as well as current flow through ion channels, including $K_{ir}2.1$, are known to govern important cellular processes, including survival, proliferation, differentiation, migration and matrix remodeling (Gautrot et al., 2014; Bates, 2015; Zaritsky et al., 2000; Chittajallu et al., 2002). However, the relationships between ion channels, FAs and cellular electrophysiology are not well understood.

Previous studies have shown that integrins and integrin-associated signaling can regulate the function of several voltage-gated ion channels through interactions with their regulatory subunits, phosphorylation, oxidative state, gene expression and trafficking (Davis et al., 2002; Becchetti et al., 2010; Arcangeli and Becchetti, 2006). In particular, trafficking has been identified as a mechanism to regulate the number of ion channels in the cardiomyocyte membrane (Boycott et al., 2013; Schumacher and Martens, 2010; Balse and Boycott, 2017). FA proteins could play a role in trafficking of $K_{ir}2.1$, since both integrins (Bridgewater et al., 2012) and $K_{ir}2.1$ channels (Ma et al., 2011) are trafficked from the Golgi to sub-membrane regions along microtubules, which are locally stabilized at FAs via phosphorylation of focal adhesion kinase (FAK, also known as PTK2) (Palazzo et al., 2004). Both integrins (Bridgewater et al., 2012) and $K_{ir}2.1$ channels (Varkevisser et al., 2013) are removed from the membrane via clathrin- or caveolae-mediated endocytotic processes that are dynamin-dependent [blocked by a dynamin 2 inhibitor (Hansen and Nichols, 2009)] and regulated by FA-associated proteins, including FAK and Src (Wang et al., 2011).

In this work, we sought to explore how changes in FA assembly within excitable cells affect $K_{ir}2.1$ membrane localization, I_{K1} amplitude, and action potential characteristics. We utilized a monoclonal line of HEK293 cells engineered to express fluorescently tagged $K_{ir}2.1$ to visualize channels, a monoclonal line of HEK293 cells ('Ex293') engineered to express $K_{ir}2.1$, the cardiac Na^+ channel $Na_v1.5$ and the gap junctional channel connexin-43 (Cx43; also known as GJA1) as a well-defined excitable cell source (Kirkton and Bursac, 2011; McSpadden et al., 2009), and neonatal rat cardiomyocytes as native excitable cells. We applied micropatterning of ECM proteins, pharmacological and environmental manipulations to alter FA size and distribution in individual cells. Combining these techniques with single-cell electrophysiology and quantitative image analysis, we provide evidence that altering FAs and integrin engagement affects $K_{ir}2.1$

Department of Biomedical Engineering, Duke University, Durham, NC 27708, USA.

*Authors for correspondence (nbursac@duke.edu; brenton.hoffman@duke.edu)

S.S., 0000-0001-5532-7818; K.E.R., 0000-0002-8191-7528; B.D.H., 0000-0003-2296-1331; N.B., 0000-0002-5688-6061

Received 17 September 2018; Accepted 31 July 2019

Journal of Cell Science (2019) 132, jcs225383. doi:10.1242/jcs.225383

membrane localization, I_{K1} amplitude, and action potential morphology in excitable cells. Furthermore, by studying $K_{ir}2.1$ turnover dynamics, we show that these channels are uniformly transported to the membrane, where they preferentially accumulate near FA-rich sites via the local inhibition of dynamin-mediated endocytosis of $K_{ir}2.1$. Overall, our studies reveal new links between the electrophysiology of ion channels and FA biology, coupling action potential dynamics to changes in the cellular environment and cytoskeletal mechanics.

RESULTS

Integrin engagement increases I_{K1} density in HEK cells

We lentivirally transduced HEK293 cells to express $K_{ir}2.1$ channels fused with tdTomato ($K_{ir}2.1$–tdTomato) and used whole-cell voltage clamp to confirm channel functionality by recording I_{K1}. The whole-cell voltage clamp recordings provide a method to specify various membrane voltage levels to a cell and quantify corresponding ion flow through membrane-bound channels (Fig. S1A,B). With expressed $K_{ir}2.1$ being the only $K_{ir}2.x$ isoform present in these cells, the amplitude of the I_{K1} current was a direct measure of the level of active $K_{ir}2.1$ channels on the plasma membrane. When the $K_{ir}2.1$–tdTomato-expressing cells were plated on fibronectin- or poly-L-lysine-coated dishes (Fig. 1A), a significantly larger I_{K1} density (current amplitude divided by membrane area) was recorded on fibronectin (Fig. 1B,C), suggesting that integrin engagement affects $K_{ir}2.1$ channels.

Constraining cell attachment area and shape reveals that there is a correlation between FA coverage and I_{K1} density

Integrin engagement in a cell is reflected by the sizes and distribution of its FAs (Schoenwaelder and Burridge, 1999). Varying the cell attachment area and shape is a common means to alter integrin engagement and FA assembly (Chen et al., 2003), which we achieved by micropatterning Ex293 cells on fibronectin islands of two defined sizes (961 μm^2 or 1600 μm^2), each in three distinct shapes (circular, square or star; Fig. S1D–G). To relate resulting changes in integrin engagement with the activity of membrane-bound $K_{ir}2.1$ channels, cells were immunostained for FA markers and imaged using confocal microscopy to determine FA coverage (the total area of FAs in microns) and I_{K1} density was measured by whole-cell voltage clamp 6 h after plating (Fig. S2A). Since FAs are complex structures, we stained multiple FA-associated proteins, including integrins, paxillin, talin and vinculin, all of which have been shown to have distinct roles in FA assembly and dynamics (Wozniak et al., 2004; Hoffman et al., 2011). Quantification of the area of active β1-integrin (Fig. S2B,C), paxillin (Fig. S2D,E), talin (Fig. S2F,G) and vinculin (Fig. 1D,E; Fig. S2H) staining revealed predominant localization of FAs in the

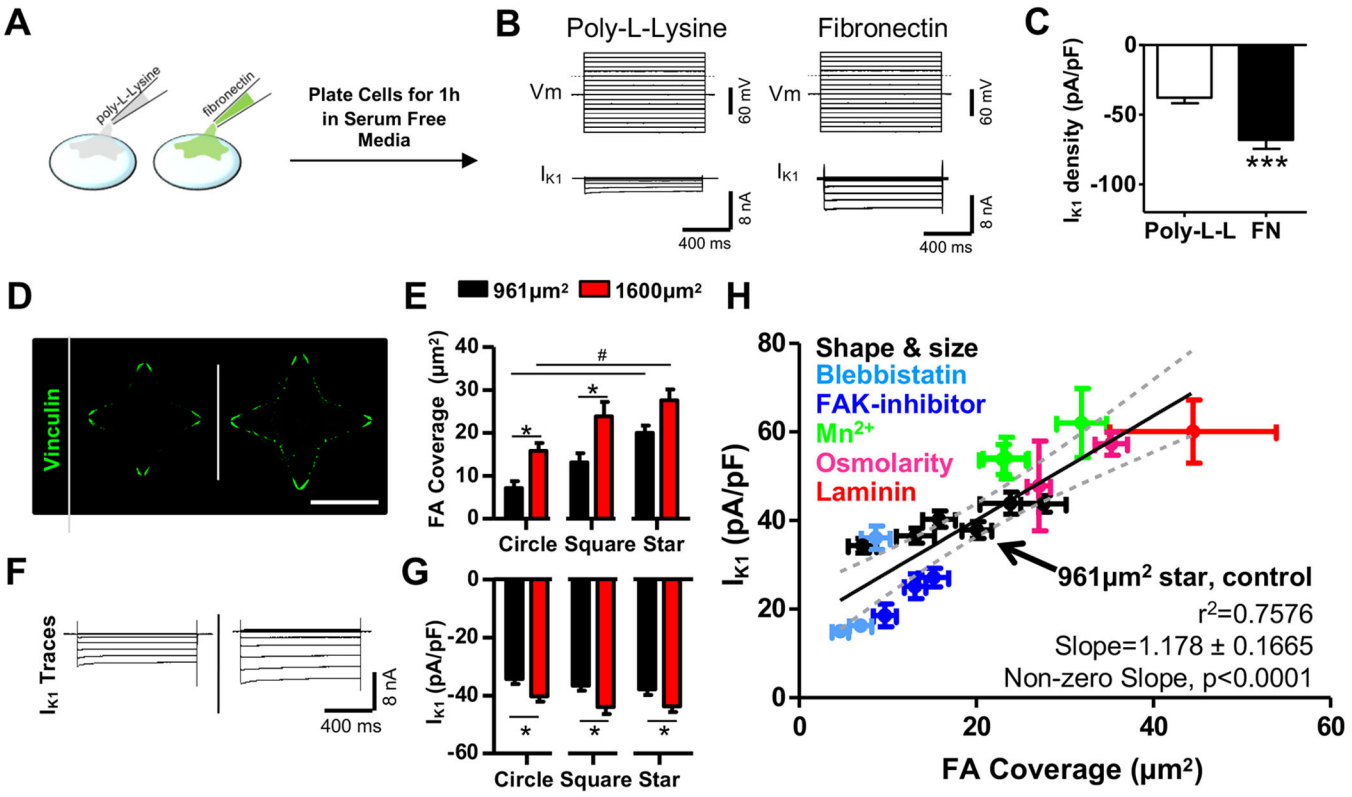

Fig. 1. Concordant changes in total FA coverage and whole-cell I_{K1} density in micropatterned Ex293 cells. (A) HEK293 cells expressing $K_{ir}2.1$ were plated on poly-L-lysine (Poly-L-L)- or fibronectin (FN)-coated glass for 1 h, and I_{K1} was assessed by whole-cell patch clamp. (B) Representative I_{K1} traces of cells plated on poly-L-lysine or fibronectin. (C) Whole-cell I_{K1} densities measured at −90 mV (n=10–13 cells per group; mean±s.e.m.). ***P<0.001 versus poly-L-lysine group (Student's t-test). (D) Representative micropatterned star-shaped Ex293 cells (left, 961 μm^2; right, 1600 μm^2) stained for vinculin (green) and (E) corresponding FA coverage quantification for cells of different shapes and sizes (n=16–27 cells per group; mean±s.e.m.; immunostained circle- and square-shaped cells are shown in Fig. S1). (F) Representative I_{K1} traces corresponding to cells shown in B. (G) Whole-cell I_{K1} densities measured at −90 mV for cells of different shapes and sizes (n=18–30 cells per group; mean±s.e.m.; representative I_{K1} traces of circle- and square-shaped cells are shown in Fig. S1). (E,G) *P<0.05; in 1600 versus 961 μm^2 cells of the same shape; #P<0.001 in star versus circle or square cells of the same patterned area (ANOVA followed by Tukey's multiple comparison test). (H) Correlation between whole-cell I_{K1} density and total FA coverage in micropatterned Ex293 cells across various cell shapes, sizes and interventions (see Figs S2, S3 and S5 for representative immunostainings, I_{K1} traces and quantifications). Scale bar: 35 μm.

Journal of Cell Science (2019) 132, jcs225383. doi:10.1242/jcs.225383

cell periphery and an increase in FA coverage with cell size, as previously reported (Kilian et al., 2010; Chen et al., 2003). The cell shape also affected FA coverage with a significant increase found in star-shaped cells. The whole-cell I_{K1} density at −90 mV increased in larger cells and was unaffected by the cell shape (Fig. 1F,G; Fig. S2I). Averaged over all shapes, a 1.66-fold larger micropatterned cell area yielded a 1.80±0.23-fold increase in FA coverage as marked by vinculin and a 1.18±0.05-fold increase in I_{K1} density, suggesting a correlation between these variables. Since all FA proteins showed similar distributions, vinculin and active β1-integrin were chosen as representative markers of FAs for subsequent studies.

Manipulations of integrin activation, FA signaling, and cell contractility concordantly regulate FA coverage and I_{K1} density

Since FA assembly is regulated by variety of cell signaling pathways (Burridge et al., 1997), we sought to probe the effects of integrin activation, FAK signaling and cell contractility on the correlation between FA coverage and I_{K1} density. To do so, cells were plated onto 961 μm^2 star-shaped islands, pharmacological agents were applied 3–6 h post plating, and FA coverage and I_{K1} density were quantified at 0, 2, 4 and 6 h post drug application (Fig. S3A). First, we activated integrins using manganese chloride ($MnCl_2$, 1 mM), which increases integrin affinity for the ECM and causes an increase in both FA area and cell traction forces (Lin et al., 2013; Bazzoni et al., 1995). The $MnCl_2$ treatment increased both FA assembly (Fig. S3B,C, to 159±27% of initial coverage; mean±s.e.m.) and I_{K1} density (Fig. S3D–F, to 166±23% of initial value). Furthermore, we disrupted FA assembly using the FAK inhibitor (FAKi) PF-573228 (100 μM), which specifically blocks the ATP-binding site at Tyr^{397} and alters the FA dynamics by blocking FAK–Src interactions (Slack-Davis et al., 2007). FA disassembly was indicated by a loss of vinculin immunostaining (to 30±2.0% of initial coverage after 6 h; Fig. S3G,H), and was accompanied by the progressive loss of I_{K1} current density (to 49±7.2% of initial value after 6 h; Fig. S3I–K). Finally, we decreased contractility in the patterned cells using the myosin II inhibitor blebbistatin (10 μM), which has previously been shown to cause a reduction in FA size and loss of vinculin at FAs (Pasapera et al., 2010). Exposure to blebbistatin caused FA disassembly (Fig. S3L,M, to 25±2.5% of initial coverage) and a reduction in I_{K1} density (Fig. S3N–P, to 40±5.1% of initial value). The FA disassembly and loss of I_{K1} were fully reversible as shown when 4 h blebbistatin treatment was followed by a 4 h drug washout (Fig. S4A–D). Moreover, the effect of blebbistatin on I_{K1} density was found to be dose dependent (Fig. S4E,F). Collectively, these results suggest that interventions that enhance FA assembly increase I_{K1} membrane density, while FA disassembly is associated with lower I_{K1} density, in a reversible and dose-dependent manner.

FA coverage and I_{K1} density are concordantly altered by changes in ECM type and membrane tension

Since different ECM proteins can engage specific types of integrins to distinctly regulate FA assembly (Friedland et al., 2009; Geiger and Yamada, 2011), we sought to determine whether the observed correlation between FA coverage and I_{K1} density is dependent on specific ECM–integrin interactions. We thus compared star-shaped cells cultured on micropatterned islands of 30 μg/ml fibronectin or 30 μg/ml laminin, and found that cells on laminin exhibited a 2.01±0.25-fold (mean±s.e.m.) increase in FA coverage (Fig. S5A,C) and consequently had a 1.76±0.20-fold higher I_{K1} density (Fig. S5B,D,E). These ECM-dependent differences may have resulted from the different types of engaged integrins, different numbers of integrin-binding sites, or both. Tension in the plasma membrane has also been shown to control integrin signaling (Bottcher and Fassler, 2014) as well as vesicle trafficking (Ferguson et al., 2017). We thus utilized hypotonic swelling to increase membrane tension (Boulant et al., 2011) by placing micropatterned cells in solutions of decreasing osmolarity for 4 h, followed by immunostaining and whole-cell patch clamp recording (Fig. S5F). Consistent with previous studies (Hirakawa et al., 2004), reduction of extracellular osmolarity resulted in increased FA coverage up to 1.76±0.20 fold (Fig. S5G,I) and a corresponding increase in I_{K1} membrane density up to 1.51±0.19 fold (Fig. S5H,J,K). We next investigated whether the observed changes in I_{K1} density induced by manipulation of integrin engagement and FA assembly are directly correlated with the altered abundance of $K_{ir}2.1$ channels at the cell membrane. For the case of FAK inhibition where I_{K1} density was gradually decreased with increased drug exposure (Fig. S3F–I), immunoblots for surface-biotinylated $K_{ir}2.1$ showed corresponding loss of channels from the membrane (Fig. S5L,M), suggesting the regulation of channel numbers at the membrane as the primary means of regulating I_{K1}.

Collectively, these results show that various means of manipulating FA assembly via extracellular and intracellular cues lead to concordant changes in the presence of $K_{ir}2.1$ channels at the membrane and, consequently, I_{K1} density. Quantitatively, when I_{K1} density was plotted against FA coverage for all studied conditions, we found strong positive linear correlation, with a Pearson's coefficient of R=0.8704 (r^2=0.7576, Fig. 1H). This conserved correlation across a diverse set of treatments further suggested that a common process may control both FA coverage and $K_{ir}2.1$ channels at the membrane.

Changes in $K_{ir}2.1$ membrane localization correlate with changes in local FA coverage

FAs are potent regulators of a number of cellular processes, including the activation of diverse signaling pathways as well as cell contractility (Parsons et al., 2010). Thus, the observed correlation between global FA coverage and I_{K1} density could be due to a cell-wide phenomenon, such as increased activity of a mobile kinase. Alternatively, the relationship could be due to a phenomenon within or proximal to FAs, potentially affecting the local recruitment of the channels. To begin to distinguish between these possibilities, we tested whether ECM-coated microspheres, which locally engage integrins, can recruit $K_{ir}2.1$ to the cell membrane (as visualized by fused tdTomato). Polystyrene microspheres (∼10 μm diameter) were coated with either poly-L-lysine, to enable electrostatic integrin-independent adhesion to cells, or fibronectin, to enable integrin-dependent adhesion. Coated microspheres were then added to cells cultured on fibronectin (Fig. 2A) and live confocal images of the membrane stained with CellMask (green) and $K_{ir}2.1$–tdTomato (red) were taken at the plane of the microspheres (Fig. 2B). At the sites where microspheres adhered to cells (appearing as circles in the confocal images), we observed enhanced recruitment of $K_{ir}2.1$–tdTomato to the microspheres for the fibronectin compared to what was seen with the poly-L-lysine coating (Fig. 2B). As a measure of $K_{ir}2.1$ membrane recruitment, we quantified the ratio of the fluorescence intensity of $K_{ir}2.1$–tdTomato to the membrane staining and found a significant increase for fibronectin-coated microspheres (Fig. 2C). These results clearly show that engaging integrins leads to the local accumulation of $K_{ir}2.1$ within the plasma membrane.

We next assessed membrane localization of $K_{ir}2.1$–tdTomato in relation to that of FAs (visualized by immunostaining for vinculin) in

Journal of Cell Science (2019) 132, jcs225383. doi:10.1242/jcs.225383

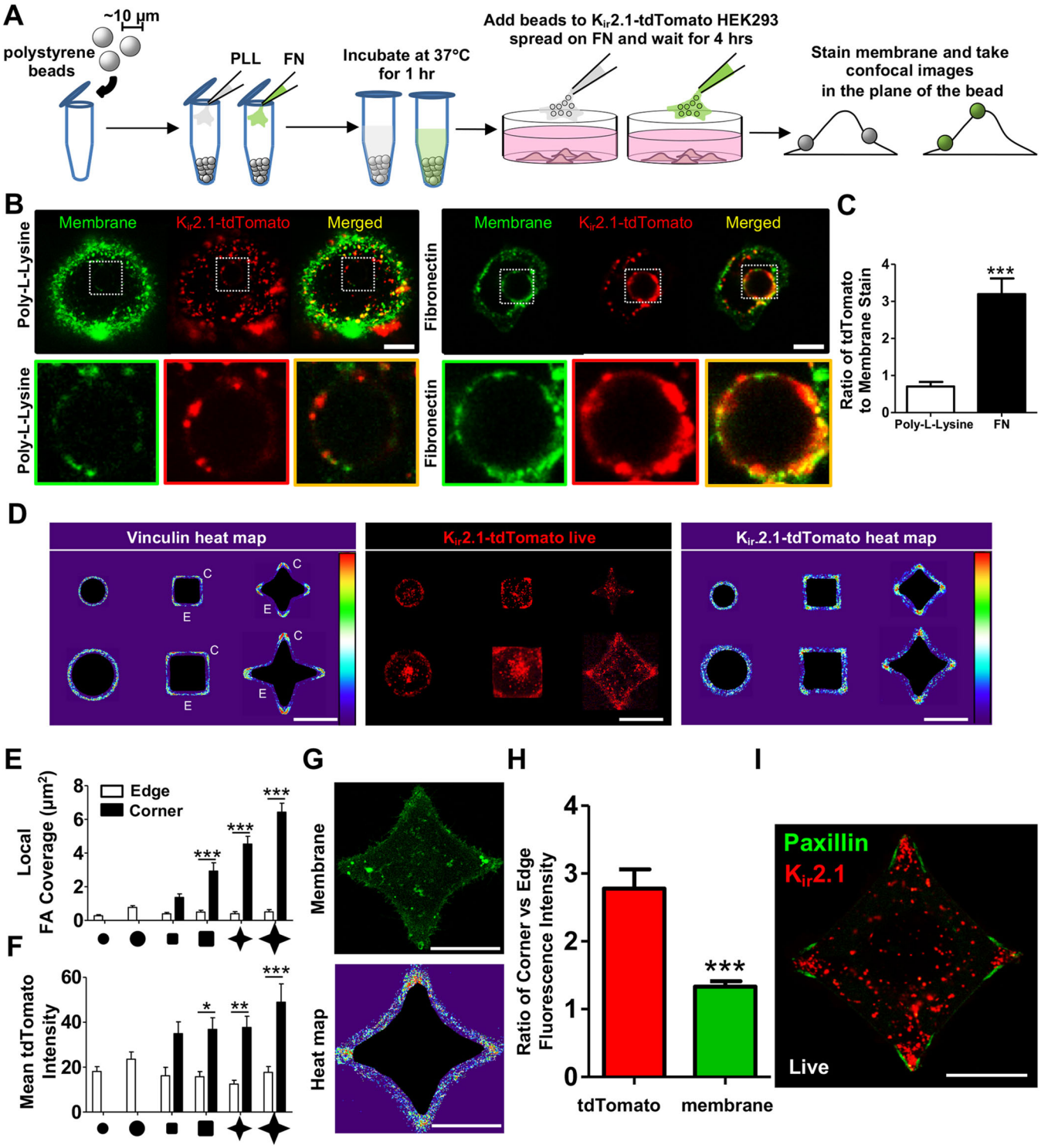

Fig. 2. See next page for legend.

micropatterned Ex293 cells of different shapes and sizes (Fig. 2D). To determine the average spatial distributions of FAs and $K_{ir}2.1$, we constructed heat maps by stacking and averaging fluorescent images from large numbers of individual micropatterned cells (Thery et al., 2006). To simplify visualization of the $K_{ir}2.1$–tdTomato near FAs at the cell periphery, we masked out the large internal pools of $K_{ir}2.1$ surrounding the nucleus (Fig. S6A), previously shown in heterologous expression systems to predominantly associate with the Golgi complex (Stockklausner et al., 2001; Hofherr et al., 2005). From vinculin heat maps (Fig. 2D, left), we observed that FA density varied along the periphery of the cells with more FAs being present at the 'corners' than 'edges' of the square- and star-shaped cells (Chen et al., 2003; Grosberg et al., 2011; Mandal et al., 2014). Similarly, the distribution of tdTomato fluorescence at the periphery of individual cells (Fig. 2D, middle) and in corresponding heat maps (Fig. 2D, right) suggested that $K_{ir}2.1$ channels were uniformly distributed in

Journal of Cell Science (2019) 132, jcs225383. doi:10.1242/jcs.225383

Fig. 2. Local recruitment of $K_{ir}2.1$ near FAs. (A) Schematic of experimental workflow whereby polystyrene microbeads were coated with poly-L-lysine or fibronectin (FN), then added to $K_{ir}2.1$–tdTomato-expressing HEK293 cells plated on FN substrates. The beads are allowed to attach to cells for 4 h; then, cell membrane was live-stained using CellMask Green and imaged in the plane of the beads with a confocal microscope. (B) Representative images in the plane of the bead for poly-L-lysine and FN coating. Bottom row, magnified images of the beads outlined in the top row by squares. Scale bars: 10 µm. (C) Quantification of ratio of tdTomato intensity per membrane stain intensity around the beads (n=11–16 beads per group; mean±s.e.m.). ***P<0.001 versus poly-L-lysine group (Student's t-test). (D) Left, heat maps of pseudocolored average vinculin intensities in stacked images of micropatterned Ex293 cells. 'Corners' and 'edges' of the shapes are denoted by 'C' and 'E', respectively; middle and right, representative images of micropatterned $K_{ir}2.1$-tdTomato HEK293 cells and corresponding heat maps of averaged tdTomato intensity in stacked images (n=21–29 cells per group). Scale bars: 35 µm. (E) Quantification of local FA coverage at corners and edges of vinculin-immunostained cells (n=16–29 cells per group; mean ±s.e.m.). (F) Mean tdTomato intensity at corners and edges of live micropatterned cells (n=21–29 cells per group; mean±s.e.m.). *P<0.05; **P<0.01; ***P<0.001 in corners versus edges (ANOVA followed by Tukey's multiple comparison test). (G) Representative image of $K_{ir}2.1$–tdTomato HEK293 cell with stained membrane (top), and corresponding heat map (n=10 cells). Scale bars: 35 µm. (H) Quantification of the ratio of corner to edge fluorescence intensity for tdTomato and membrane stain (n=10–21 cells per group; mean±s.e.m.). ***P<0.001 versus tdTomato group (Student's t-test). (I) Representative image of live HEK293 cell co-expressing $K_{ir}2.1$–tdTomato and EGFP–paxillin. Scale bar: 35 µm.

membranes of circular cells but were more abundant at corners than edges in square- and star-shaped cells, concordant with the spatial distribution of FAs. This observation was further corroborated by quantifying local (edge and corner) abundances of FAs (protein coverage, Fig. 2E and Fig. S6) and $K_{ir}2.1$ (tdTomato intensity, Fig. 2F), as both showed similar cell shape and size dependences. We then labeled the membrane of star-shaped $K_{ir}2.1$–tdTomato HEK293 cells with CellMask Green (Fig. 2G) and quantified the corner versus edge fluorescence intensity ratio for tdTomato and membrane staining. Compared to a 2.9-fold increase in tdTomato intensity at corner versus edges, the membrane staining intensity was increased only 1.3-fold (Fig. 2H), demonstrating that $K_{ir}2.1$ channels are preferentially enriched within the membrane at cell corners. Furthermore, we expressed EGFP fused to the N-terminus of paxillin (EGFP–paxillin) in $K_{ir}2.1$-tdTomato cells to directly visualize the potential colocalization of $K_{ir}2.1$ and FAs in live cells. Confocal imaging suggested that channels accumulate in proximity to, but not within, FAs (Fig. 2I). Overall, the ECM-coated microsphere experiments, quantitative analyses of local FA and $K_{ir}2.1$ abundances, and the assessment of $K_{ir}2.1$ and paxillin co-localization suggest that $K_{ir}2.1$ localization in the cell membrane is stimulated by local integrin engagement, but likely without the physical interaction of the channel with FAs.

Functional consequences of altered FA and membrane $K_{ir}2.1$ localization

We assessed the functional consequences of $K_{ir}2.1$ recruitment proximal to FAs by performing cell-attached patch clamp at corners and edges of micropatterned Ex293 cells (Fig. 3A,B). The recorded local I_{K1} strongly correlated with the mean $K_{ir}2.1$–tdTomato intensity, with a Pearson's coefficient of R=0.963 (r^2=0.9287, Fig. 3C), suggesting that the quantified tdTomato labeled active $K_{ir}2.1$ channels reside on the membrane. Next, we sought to manipulate FA assembly in a micropatterning-independent manner and probe the local correlations between FA coverage and I_{K1} at the cell edges and corners. To do so, we applied 100 µM FAKi for 2 h, which shifted the FA distribution in star-shaped cells from being enriched at the corners to being relatively uniform along the cell boundary (Fig. 3D, left). This change in FA distribution coincided with the loss of the $K_{ir}2.1$ enrichment at corners and the emergence of an apparently homogenous channel distribution (Fig. 3D, right). Quantitative image analysis and cell-attached patch clamp revealed that the uniform FA redistribution along the cell boundary (Fig. 3E) resulted in the decrease of I_{K1} amplitude at the corners and increase at the edges (Fig. 3F). Plotting the local I_{K1} amplitude versus the corresponding local FA coverage across different conditions showed a strong linear correlation (r^2=0.8485, Fig. 3G), confirming that active $K_{ir}2.1$ channels are enriched near FAs and suggesting that a locally regulated process mediates the functional relationship between FA assembly and I_{K1}.

In excitable cells, I_{K1} plays important roles in regulating the resting membrane potential (RMP) and cell excitability by influencing both Na^+ current (I_{Na}) availability and action potential (AP) threshold (Kléber and Rudy, 2004; Miake et al., 2003). Additionally, the outward portion of I_{K1} influences the terminal phase of action potential repolarization and AP duration (APD). The use of monoclonal excitable Ex293 cells in our studies enabled us to further assess potential roles of FA-mediated $K_{ir}2.1$ regulation in AP shape and excitability. By performing voltage- and current-clamp recordings in star-shaped Ex293 cells of different size, we found that larger cells had higher outward peak I_{K1} density (Fig. 3H), shorter APD (Fig. 3I,J) and similar RMP (Fig. 3I,K) compared to smaller cells. Furthermore, compared to cells of the same size and shape, cultured on fibronectin islands, Ex293 cells cultured on laminin exhibited a higher outward peak I_{K1} density (Fig. 3L), reduced APD (Fig. 3M,N) and hyperpolarized RMP (Fig. 3M,O). Overall, these results suggest that intracellular and extracellular signals regulating integrin engagement and FA assembly may also have important roles in controlling the electrophysiological properties of excitable cells and tissues.

Membrane localizations of $Na_v1.5$ and Cx43 appear independent of integrin engagement

Since previous studies have shown that $Na_v1.5$ and $K_{ir}2.1$ have a parallelism in expression (Milstein et al., 2012; Utrilla et al., 2017; Ponce-Balbuena et al., 2018), we next explored whether the cell shape and size affect membrane localization and activity of $Na_v1.5$ channels by immunostaining and electrophysiological analysis, respectively. We found that, unlike $K_{ir}2.1$, $Na_v1.5$ exhibited no preferential localization in the corners versus edges of star-shaped Ex293 cells (Fig. S7A,B). Interestingly, the whole-cell I_{Na} density (Fig. S7C,D) and action potential upstroke (Fig. S7E) were still increased in larger Ex293 cells, collectively suggesting that while the numbers of active $Na_v1.5$ channels on cell membrane may be related to the numbers of active $K_{ir}2.1$ channels, the membrane distribution of $Na_v1.5$ does not appear to be affected by changes in either local integrin engagement or $K_{ir}2.1$ distribution. Furthermore, similar to $Na_v1.5$, immunostained Cx43 in star-shaped Ex293 cells exhibited a uniform membrane distribution (Fig. S7F,G), indicating the lack of local regulation by engaged integrins or $K_{ir}2.1$.

Engaging integrins provides inhibitory signals to $K_{ir}2.1$ endocytosis

Since $K_{ir}2.1$ channels are trafficked to the membrane (Leonoudakis et al., 2004; Balse et al., 2012), we evaluated the possibility that FAs regulate $K_{ir}2.1$ localization and distribution by modulating channel trafficking. To probe FAs, we imunofluorescently labeled active β1-integrin, representing the transmembrane component of the FA.

Journal of Cell Science (2019) 132, jcs225383. doi:10.1242/jcs.225383

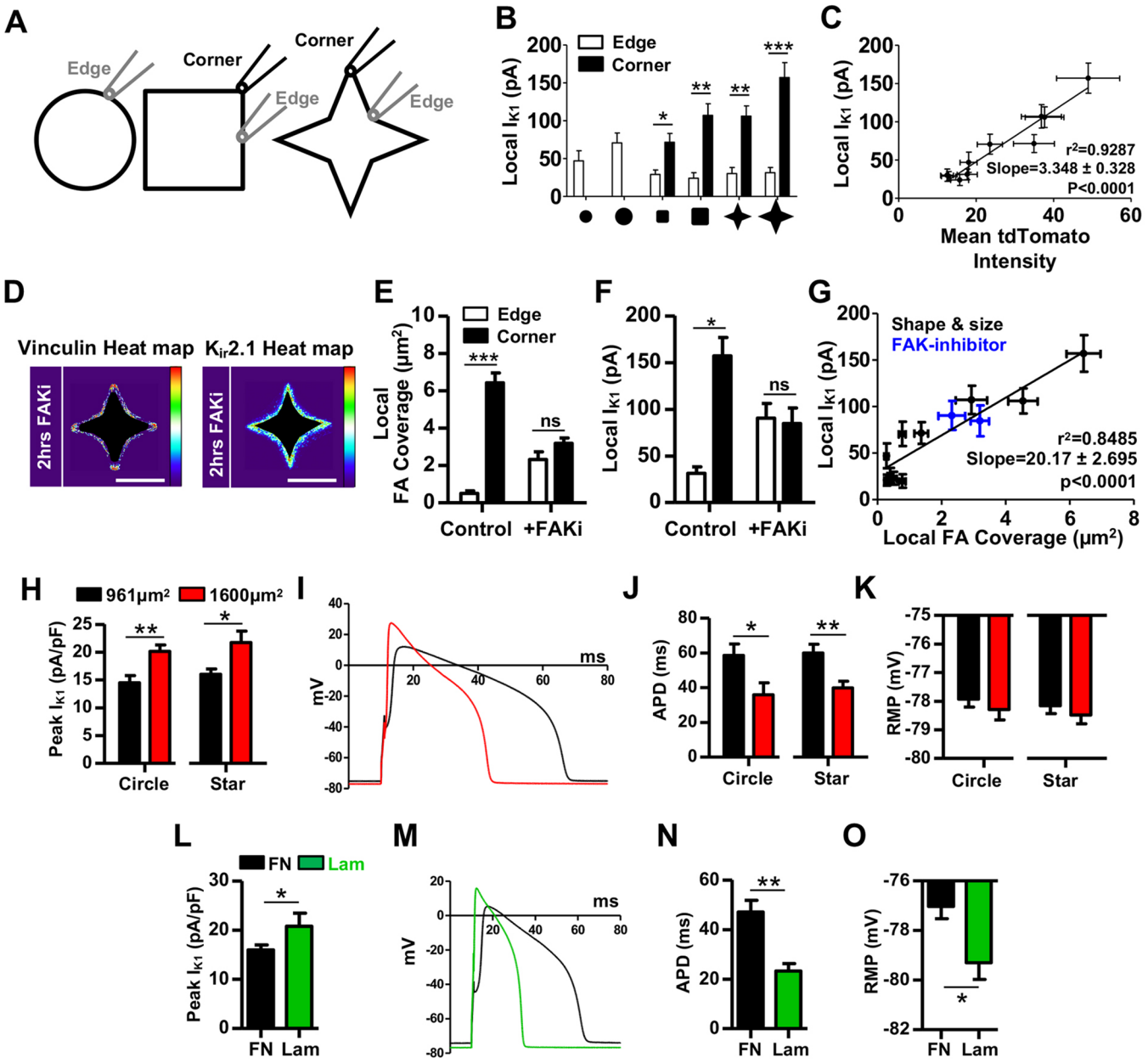

Fig. 3. Concordant changes in local FA coverage and I_{K1} in micropatterned Ex293 cells regulate action potential shape. (A) Schematics of 'corner' and 'edge' regions of micropatterned cells used for local FA coverage quantification and cell-attached patch clamp recordings. (B) Local corner and edge I_{K1} amplitudes measured at −90 mV in micropatterned Ex293 cells (n=5–20 cells per group; mean±s.e.m.). (C) Correlation between local I_{K1} amplitude and local tdTomato mean intensity in micropatterned cells with different shapes and sizes. (D) Heat maps of averaged vinculin (left) and tdTomato (right) intensities in stacked images of 1600 μm² star-shaped Ex293 cells treated for 2 h with FAK inhibitor (n=15 cells per group). Scale bars: 35 μm. Control heat maps are presented in Fig. 2D. (E,F) Corresponding quantifications of local FA coverage (E, n=13–29 cells per group; mean±s.e.m.) and local I_{K1} amplitude measured at −90 mV (F, n=5–12 cells per group; mean±s.e.m.). *P<0.05; **P<0.01; ***P<0.001 for corner versus edge in cells of the same shape and size (ANOVA followed by Tukey's multiple comparison test); ns, not significant. (G) Correlation between local I_{K1} amplitude and local FA coverage in micropatterned Ex293 cells with different shapes, sizes and FAK inhibition. (H) Quantification of peak outward I_{K1} density measured in circle- and star-shaped, 961 and 1600 μm² Ex293 cells (n=22–30 cells per group; mean±s.e.m.). (I) Representative action potential traces in 961 and 1600 μm² cells and (J) corresponding quantification of APDs (n=6–9 cells per group; mean±s.e.m.) and (K) RMPs (n=22–30 cells per group; mean±s.e.m.). (H,J) *P<0.05; **P<0.01 for 1600 versus 961 μm² cells of the same shape (ANOVA followed by Tukey's multiple comparison test). (L) Quantification of peak outward I_{K1} density measured in 961 μm² star-shaped Ex293 cells cultured on fibronectin (FN) or laminin (Lam) micropatterns (n=10–12 cells per group; mean±s.e.m.). (M) Representative AP traces, and (N) corresponding quantification of action potential duration at 80% repolarization (APD; n=7–17 cells per group; mean±s.e.m.) and (O) resting membrane potential (RMP; n=10–12 cells per group; mean±s.e.m.). (L,N,O) *P<0.05; **P<0.01 for Lam versus FN group (Student's t-test).

Active β1-integrin immunostaining led to a small amount of labeling of the nucleus that was not observed in any of the other FA markers. Therefore, we regarded this nuclear labeling as artifactual and excluded it from the visualization and quantification (using masks from DAPI stainings). For this set of experiments, we first halted microtubule (MT)-dependent forward and reverse trafficking of K_{ir}2.1 (Loewen et al., 2009) in micropatterned HEK cells by using the microtubule-destabilizing agent Nocodazole (Noco,

Journal of Cell Science (2019) 132, jcs225383. doi:10.1242/jcs.225383

12 µM). This treatment yielded a transient increase in FA coverage within 2 h, but no statistically significant difference in FA coverage after 6 h (as determined by active β1-integrin labeling, Fig. 4A,B). No statistically significant increase was observed in I_{K1} density (Fig. 4C). Given a previously demonstrated relationship between MT disruption and enhanced FA assembly (Enomoto, 1996), we simultaneously treated cells with 12 µM nocodazole and 100 µM FAKi (Noco+FAKi), which resulted in the gradual disassembly of FAs (Fig. 4A,B) and reduction of I_{K1} density (Fig. 4C). Previous work has shown that MT-dependent trafficking is required for the initial delivery of $K_{ir}2.1$ to the membrane and recycling of $K_{ir}2.1$ (Loewen et al., 2009). Our results make evident that MTs do not govern the selective accumulation of $K_{ir}2.1$ near FAs and suggest that the membrane localization of the channel may be locally regulated by FAs.

Thus, we next examined the potential roles of FAs in the insertion and retention of channels at the membrane as means to govern the local accumulation of $K_{ir}2.1$. Specifically, we investigated whether dynamin-dependent endocytosis mediates the relationship between FAs and $K_{ir}2.1$. Dynamin is a protein required for the final membrane scission to complete endocytosis that is inhibited by a small molecule, Dynasore (Dyn; Macia et al., 2006). A 6-h treatment of Ex293 cells with 25 µM Dyn yielded a progressive increase in both active β1-integrin coverage (Fig. 4D,E; $P<0.001$) and I_{K1} density (Fig. 4F; $P<0.001$), an expected result since dynamin mediates internalization of integrins (Alanko et al., 2015)

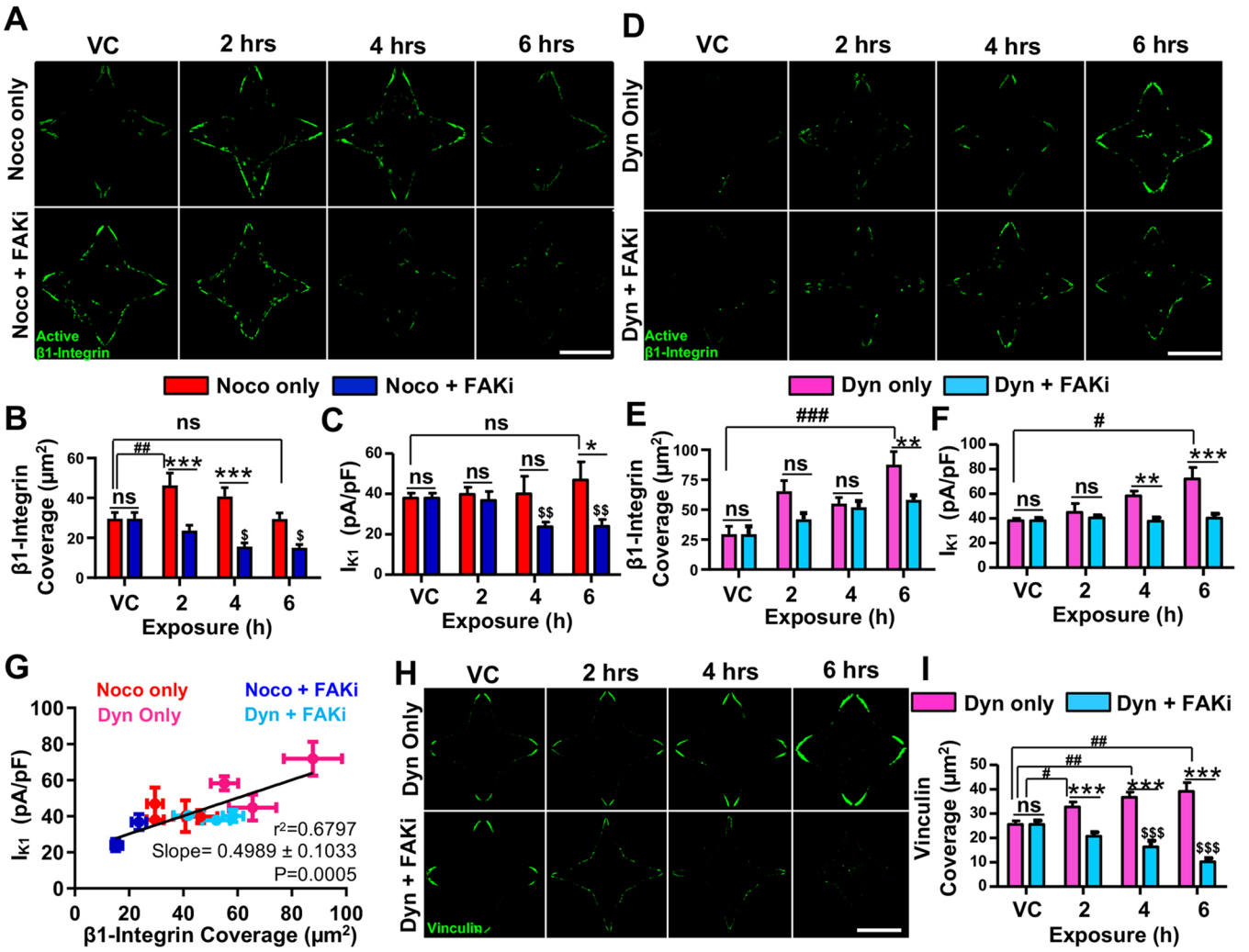

Fig. 4. Effects of microtubular trafficking and endocytosis on FAKi-induced I_{K1} reduction in micropatterned Ex293 cells. (A) Representative images of micropatterned Ex293 cells immunostained for active β1-integrin after exposure to 12 µM Nocodazole (Noco, top) or 100 µM FAK-inhibitor (FAKi)+12 µM Nocodazole (Noco+FAKi, bottom) for 2, 4 or 6 h. 'VC' represents a 6-h exposure to vehicle control. (B,C) Corresponding quantifications of active β1-integrin coverage (B, n=10 cells per group; mean±s.e.m.) and I_{K1} density measured at −90 mV (C, n=5–14 cells per group; mean±s.e.m.). (D) Representative images of Ex293 cells stained for active β1-integrin after exposure to 25 µM Dynasore (Dyn, top) or 100 µM FAK-inhibitor (FAKi)+25 µM Dynasore (Dyn+FAKi, bottom) for 2, 4 or 6 h. (E,F) Corresponding quantifications of active β1-integrin coverage (E, n=10 cells cells per group; mean±s.e.m.) and I_{K1} density measured at −90 mV (F, n=6–20 cells per group; mean±s.e.m.). (G) Correlation between I_{K1} density and active β1-integrin coverage for different interventions. (H) Representative images of Ex293 cells stained for vinculin after exposure to 25 µM Dynasore (Dyn, top) or 100 µM FAK-inhibitor (FAKi)+25 µM Dynasore (Dyn+FAKi, bottom) for 2, 4 or 6 h. (I) Corresponding quantifications of total FA coverage in Ex293 cells (n=6–13 cells per group; mean±s.e.m.). $^{*}P<0.05$, $^{**}P<0.01$, $^{***}P<0.001$ for without FAKi versus with FAKi; $^{\#}P<0.05$, $^{\#\#}P<0.01$, $^{\#\#\#}P<0.001$ for Noco treatment compared to vehicle control and Dyn treatment compared to vehicle control; $^{\$}P<0.05$, $^{\$\$}P<0.01$, $^{\$\$\$}P<0.001$ for Noco+FAKi treatment compared to vehicle control and Dyn+FAKi treatment compared to vehicle control. Note: vehicle controls are pooled for panels B–F (with and without FAKi treatment represents the same data for 'VC'); ns, not significant (ANOVA followed by Tukey's multiple comparison test). Scale bars: 20 µm.

Journal of Cell Science (2019) 132, jcs225383. doi:10.1242/jcs.225383

and $K_{ir}2.1$ (Varkevisser et al., 2013). To probe the role of dynamin in FAKi-induced removal of integrin and $K_{ir}2.1$ from the membrane, FAKi-treated Ex293 cells were co-treated with Dyn, which prevented the FAKi-induced loss of active β1-integrin (Fig. 4D,E) and I_{K1} (Fig. 4F), and maintained the correlation between FA coverage and I_{K1} density (Fig. 4G). Given that adding Dyn to FAKi was the first intervention to prevent decrease in I_{K1}, we immunostained for vinculin (Fig. 4H) and found that the Dyn+FAKi treatment yielded progressive loss of vinculin coverage (Fig. 4I), indicating that FA disassembly was still occurring under these conditions without loss of active β1-integrin coverage. These results suggested that dynamin-dependent stabilization of active integrins on the membrane results in $K_{ir}2.1$ localization near FAs leading to a local increase in I_{K1}. Engaging integrins prevents endocytosis of $K_{ir}2.1$ channels, while removing active integrins from the membrane is associated with internalization of $K_{ir}2.1$ channels and an I_{K1} decrease.

Rate of $K_{ir}2.1$ delivery to membrane is spatially uniform, while rate of $K_{ir}2.1$ endocytosis is dependent on FAs

Next, we sought to determine the turnover rate of $K_{ir}2.1$ channels at cell corners, where FAs are large, and edges, where FAs are small through fluorescence recovery after photobleaching (FRAP) (Fig. 5A). After local bleaching of $K_{ir}2.1$–tdTomato in star-shaped HEK293 cells, fluorescence recovered at a slower rate at the cell corners (τ_c=158±35 s) than edges (τ_c=70±10 s, Fig. 5B,C). Cell corners also exhibited a smaller mobile fraction, M_f, of $K_{ir}2.1$ channels compared to cell edges (Fig. 5B,C), indicating the stabilization of $K_{ir}2.1$ in the membrane at the FA-rich sites. To test the role of dynamin activity in $K_{ir}2.1$ turnover dynamics, we performed FRAP experiments in $K_{ir}2.1$–tdTomato-expressing cells that had been treated with 25 µM Dyn for 4 h (Fig. 5D). Since inhibition of endocytosis by Dyn leads to the membrane accumulation of $K_{ir}2.1$ (Fig. 4F), as reflected in an increased I_{K1} density, this experiment preferentially probed the rate of forward transport of the channel to the membrane. Endocytosis inhibition by Dyn thus revealed that channel forward transport rates are the same at cell corners and edges (Fig. 5E,F). The mobile channel fraction remained smaller at corners than edges (Fig. 5E,F), likely due to the preserved spatial distribution of FAs (Fig. 4D). Differences in the initial data points in the FRAP curves were due to variable levels of bleaching. Together, these data are consistent with the model where $K_{ir}2.1$ channels are spatially uniformly delivered to the cell membrane, then non-uniformly endocytosed in an FA-dependent and dynamin-dependent manner. This spatially non-uniform endocytosis causes a heterogeneous distribution of $K_{ir}2.1$ channels along the membrane with more channels localizing near larger FA complexes with increased integrin engagement.

Neonatal rat ventricular myocytes also exhibit concordant changes in FA coverage and I_{K1} density, both globally and locally

We next explored whether the strong correlation between integrin engagement and I_{K1} density observed in engineered HEK293 cells is also found in native excitable cells – neonatal rat ventricular myocytes (NRVMs). The NRVMs micropatterned on circular-, square- and star-shaped fibronectin islands displayed similarly distributed but more abundant FAs (Fig. 6A) than those in HEK293 cells, with larger NRVMs exhibiting both larger total FA coverage (Fig. 6B) and endogenous I_{K1} density (Fig. 6C). Averaged over all

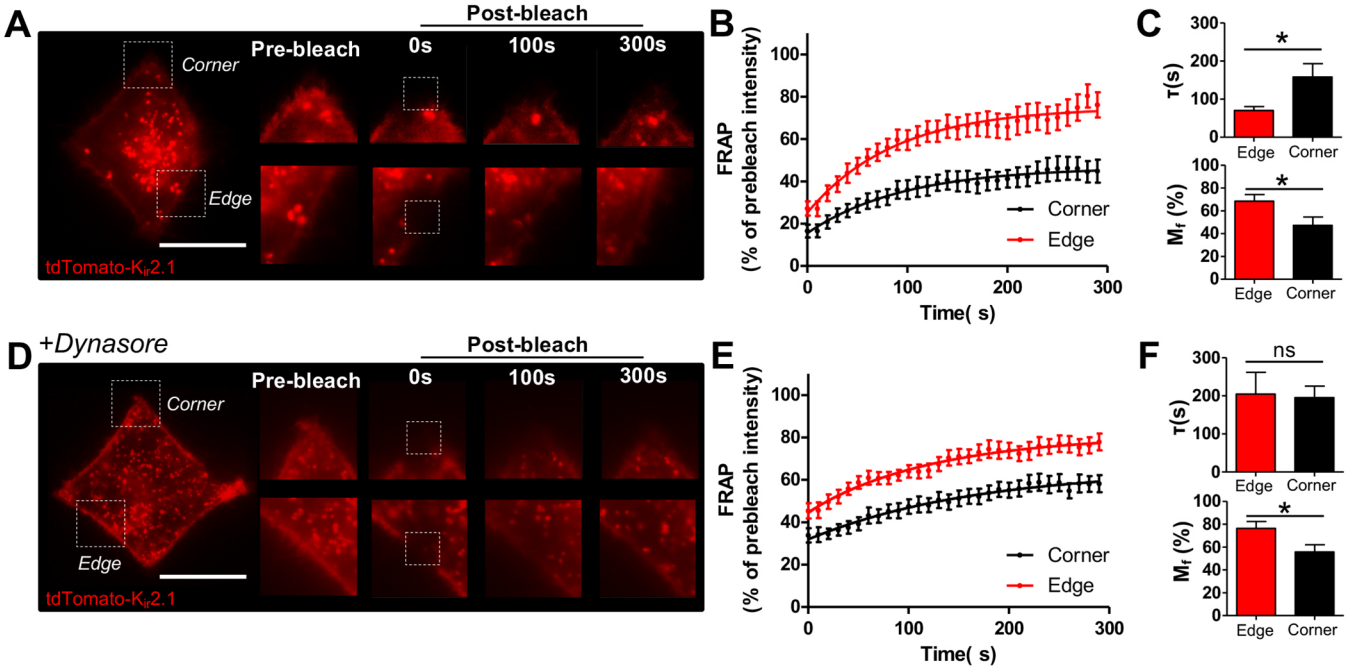

Fig. 5. Insertion and internalization of $K_{ir}2.1$ into the membrane of micropatterned HEK293 cells. (A) Representative snapshots of bleach-corrected $K_{ir}2.1$–tdTomato live fluorescence in micropatterned HEK293 cells shown pre-bleaching and at various times post-bleaching. White boxes indicate edge and corner regions used for FRAP analysis. (B) Experimental data and single-exponential fits of $K_{ir}2.1$–tdTomato fluorescence recovery in the corner versus edge regions. (C) Corresponding quantifications of time constant of recovery (τ, top) and mobile fraction (M_f, bottom n=19 cells per group; mean±s.e.m.). (D) Representative snapshots of bleach-corrected $K_{ir}2.1$–tdTomato live fluorescence in micropatterned HEK293 cells treated with 25 µM dynasore for 4 h shown pre-bleaching and at various times post-bleaching. Boxes indicate edge and corner regions used for FRAP analysis. (E) Experimental data and single-exponential fits of $K_{ir}2.1$–tdTomato fluorescence recovery in the corner versus edge regions. (F) Corresponding quantifications of time constant of recovery (τ, top) and mobile fraction (M_f, bottom, n=17 cells per group; mean±s.e.m.). *P<0.05 for corner versus edge (Student's t-test); ns, not significant. Scale bars: 35 µm.

Journal of Cell Science (2019) 132, jcs225383. doi:10.1242/jcs.225383

shapes, a 1.66-fold larger micropatterned NRVM area yielded a 1.35-fold increase in FA coverage marked by vinculin and a 1.59-fold higher I_{K1} density. Furthermore, we applied selected perturbations of FA assembly in NRVMs and recorded the resulting changes in endogenous I_{K1} density (Fig. 6D–F). Application of 10 µM Blebbistatin for 6 h resulted in a breakdown of actin stress fibers as well as decrease in FA coverage and I_{K1} density to 71% and 47% of original values, respectively. Similarly,

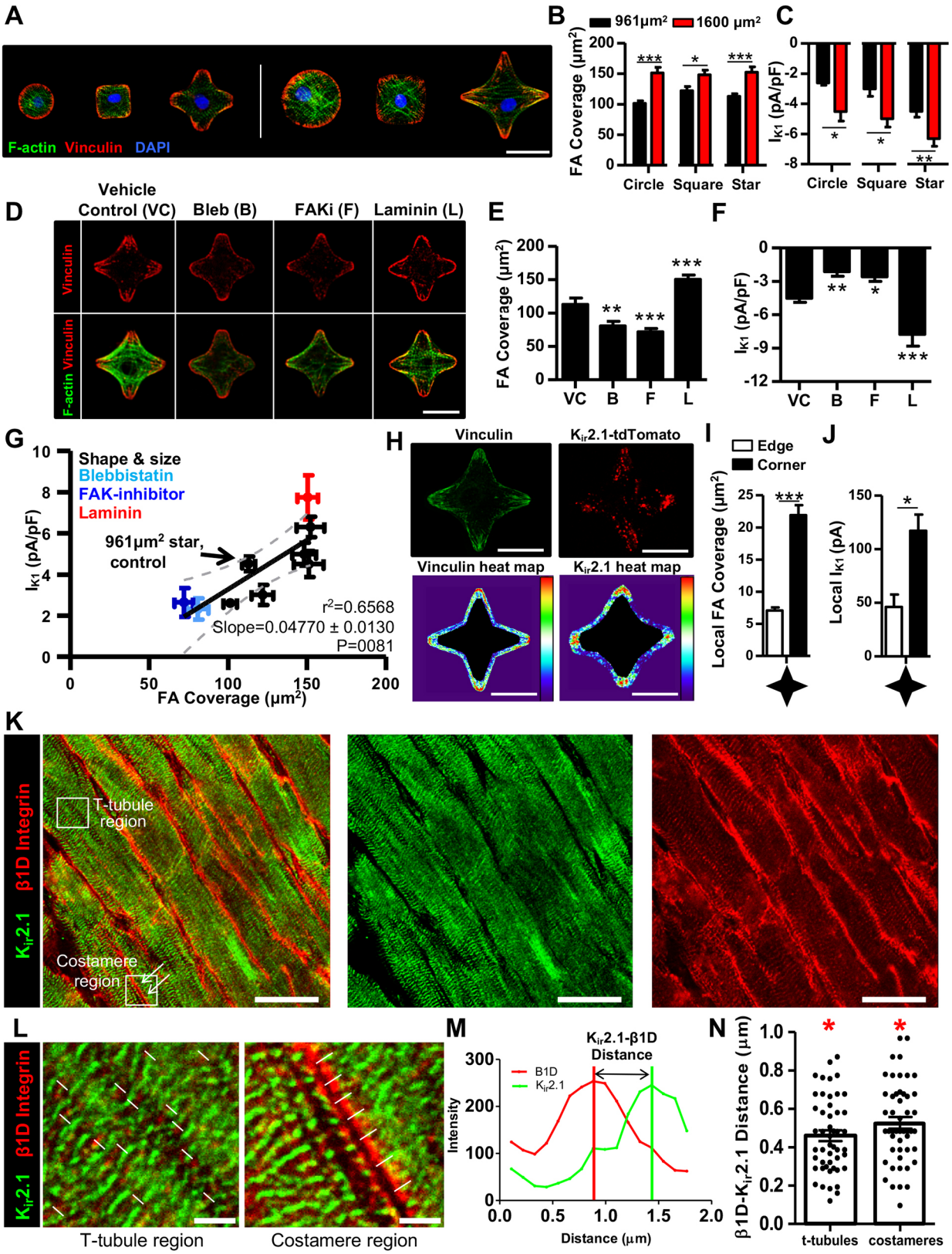

Fig. 6. See next page for legend.

Journal of Cell Science (2019) 132, jcs225383. doi:10.1242/jcs.225383

Fig. 6. Role of integrin engagement in membrane localization and function of $K_{ir}2.1$ in rat cardiomyocytes. (A) Representative images of micropatterned NRVMs stained for vinculin (red), actin (green) and nuclei (DAPI, blue). Scale bar: 35 µm. (B,C) Corresponding quantifications of total FA coverage marked by vinculin (B, *n*=18–26 cells per group; mean±s.e.m.) and whole-cell I_{K1} density measured at −90 mV (C, *n*=7–14 cells per group; mean ±s.e.m.). **P*<0.05; ***P*<0.01; ****P*<0.001 for 1600 versus 961 µm^2 cells of the same shape (ANOVA followed by Tukey's multiple comparison test). (D) Representative images of micropatterned NRVMs stained for vinculin (red) and actin (green) after exposure to vehicle control for 6 h (VC) or 6 h of exposure to 10 µM Blebbistatin (Bleb, 'B') or 100 µM FAKi ('F'), or plating on laminin ('L'). Scale bar: 20 µm. (E,F) Corresponding quantifications of total FA coverage marked by vinculin (E, *n*=7–15 cells per group; mean±s.e.m.) and whole-cell I_{K1} density measured at −90 mV (F, *n*=6–17 cells per group; mean±s.e.m.). **P*<0.05; ***P*<0.01; ****P*<0.001 versus control (ANOVA followed by Dunnett's test). (G) Correlation between whole-cell I_{K1} density and total FA coverage in micropatterned NRVMs across various cell shapes, sizes and interventions. (H) Representative images of micropatterned cells immunostained for vinculin or $K_{ir}2.1$–tdTomato and corresponding heat maps of average fluorescence intensity in stacked images (*n*=10–15 cells per group). Scale bar: 35 µm. (I,J) Corresponding quantifications of local FA coverage (I, *n*=10 cells per group; mean±s.e.m.) and local I_{K1} amplitude measured at −90 mV (J, *n*=3–5 cells per group; mean±s.e.m.). **P*<0.05; ****P*<0.001 for corner versus edge (Student's *t*-test). (K) Representative adult rat ventricular section immunostained for β1D integrin (red) and $K_{ir}2.1$ (green) with examples of t-tubule and costameric (shown with white arrows) regions denoted with white squares. Scale bars: 20 µm. Note the lack of overlap between red and green fluorescence. (L) Magnified images of the t-tubule (left) and costamere (right) regions from K. Scale bars: 5 µm. (M) Representative green and red fluorescence intensity profiles along one of the white lines shown in L used to quantify peak-to-peak distances between $K_{ir}2.1$ and β1D labels. (N) Quantification of the distance between $K_{ir}2.1$ and β1D integrin puncta in t-tubule and costamere regions (*n*=49 fluorophore pairs per group; mean ±s.e.m.). **P*<0.0001 versus 0 µm distance (one-sample *t*-test).

100 µM FAKi yielded a loss of actin stress fibers, accompanied by a decrease in FA coverage and I_{K1} density to 64% and 57% of original values. NRVMs were then plated on star-shaped islands of laminin, and found to have increased FA coverage by 33% and I_{K1} density by 71%. Similar to engineered HEK293 cells, plotting the endogenous I_{K1} density against the total FA coverage for all studied conditions in NRVMs yielded a positive correlation (r^2=0.6568, Fig. 6G). Moreover, when 1600 µm^2 star-shaped NRVMs were transduced with $K_{ir}2.1$–tdTomato, the channels localized at a higher density in cell corners than edges (Fig. 6H), consistent with the higher local FA coverage (Fig. 6I). As in HEK293 cells, the local I_{K1} amplitude in these NRVMs was found to be higher in cell corners than edges (Fig. 6J). Together, these results indicate that, similar to what is found for Ex293 cells, interventions that alter integrin engagement and FA assembly concordantly alter $K_{ir}2.1$ and I_{K1} in neonatal cardiomyocytes, as an example of native excitable cells.

$K_{ir}2.1$ and integrins in adult rat ventricle consistently localize proximal to each other

Finally, we explored the spatial relationships between $K_{ir}2.1$ channels and β1D integrins (the β1 isoform found in cardiac tissue) in adult rat ventricles through immunostaining and image analysis. Specifically, we assessed how the two proteins localize in both the t-tubule (Kostin et al., 1998; Vaidyanathan et al., 2013; Israeli-Rosenberg et al., 2015; Okada et al., 2013) and costamere (Clark et al., 2001; Samarel, 2005) regions of cardiomyocyte membrane (Fig. 6K,L). In agreement with the finding in HEK293 cells (Fig. 2I), the $K_{ir}2.1$ and β1D immunofluorescence did not overlap, but were consistently localized proximal to each other throughout the cardiomyocyte at an average distance of 0.494 ±0.021 µm (Fig. 6M,N). This result supported the possibility that signals for integrin engagement may also regulate membrane localization of $K_{ir}2.1$ in adult cardiomyocytes.

DISCUSSION

Our studies suggest a fundamental link between FA assembly and membrane localization of $K_{ir}2.1$ channels (summarized in Fig. 7). By employing cell micropatterning techniques and targeted pharmacological interventions, we show that increasing integrin engagement (and FA coverage) in cells proportionally increases the abundance of functional $K_{ir}2.1$ channels at the cell membrane (Fig. 1). The microsphere experiments confirmed that the *de novo* engagement of integrins can recruit $K_{ir}2.1$ channels to accumulate at the sites of newly formed FAs (Fig. 2). Local variations in FA coverage strongly correlated with local membrane abundance of $K_{ir}2.1$, such as at corners versus edges of micropatterned cells (Fig. 2), indicating a local mechanism for channel recruitment leading to changes in local and global I_{K1} (Fig. 3). In contrast, the membrane distribution of overexpressed $Na_v1.5$ did not appear to be correlated with local integrin engagement (Fig. S7A). Use of pharmacological inhibitors to probe the involvement of key mechanisms of channel trafficking revealed that the internalization of $K_{ir}2.1$ during FA disassembly is MT-independent but requires dynamin (Fig. 4). FRAP analysis of $K_{ir}2.1$ turnover suggested that the channel is uniformly transported to the membrane, but is less readily endocytosed from the membrane near sites of strong integrin engagement (large FA complexes, Fig. 5). Overall, we propose that, through this mechanism, a spatially heterogeneous distribution of FAs in a cell contributes to a spatially heterogeneous distribution of $K_{ir}2.1$ channels at the cell membrane, while altering the global levels of integrin engagement can serve to alter whole-cell I_{K1} density and AP shape, both in engineered (Fig. 3) and primary (Fig. 6) excitable cells. The close spatial localization of $K_{ir}2.1$ channels and β1D integrins in rat ventricles (Fig. 6) further indicated the potential relevance of these findings for adult cardiomyocytes *in vivo*.

Mechanistically, our results suggest that $K_{ir}2.1$ membrane localization is at least in part regulated by a local diffusible signal generated by integrin engagement, as the absence of colocalization of $K_{ir}2.1$ with paxillin (Fig. 2I) argues against direct interactions of the channel with FA proteins. In principle, this diffusible signal could either affect dynamin activity, $K_{ir}2.1$ activity, or the interaction of dynamin and $K_{ir}2.1$. The direct regulation of dynamin seems unlikely, as dynamin plays a crucial role in the endocytosis of integrins (Bridgewater et al., 2012) and other membrane receptors (Faelber et al., 2012) within and proximal to FAs. Previous studies have demonstrated that phosphorylation of $K_{ir}2.1$ can inhibit its activity (Wischmeyer et al., 1998; Vega et al., 2009). However, the strong correlation between I_{K1} and the intensity of $K_{ir}2.1$–tdTomato is most consistent with the channel being constitutively active at the membrane and inconsistent with a significant role of post-translational regulation. Therefore, we postulate that integrin-mediated diffusible signals interfere with the interaction between $K_{ir}2.1$ and dynamin to prevent removal of channel from the membrane. Filamin A and dystroglycan have been reported to interact with $K_{ir}2.1$ as well as dynamin (Noam et al., 2014; Zhan et al., 2005; Sampson et al., 2003). These proteins, which are likely proximal to FAs due to their localization to the actin cortex, could act as $K_{ir}2.1$-regulating scaffolding proteins, and their roles in the endocytosis of $K_{ir}2.1$ channels remain to be studied.

$K_{ir}2.1$ is not a stretch-gated channel, as shown by its insensitivity to gadolinium or lack of immediate response to 10–30 min of hypo-osmotic shock (Ji et al., 1998). However, the application of fluid

Journal of Cell Science (2019) 132, jcs225383. doi:10.1242/jcs.225383

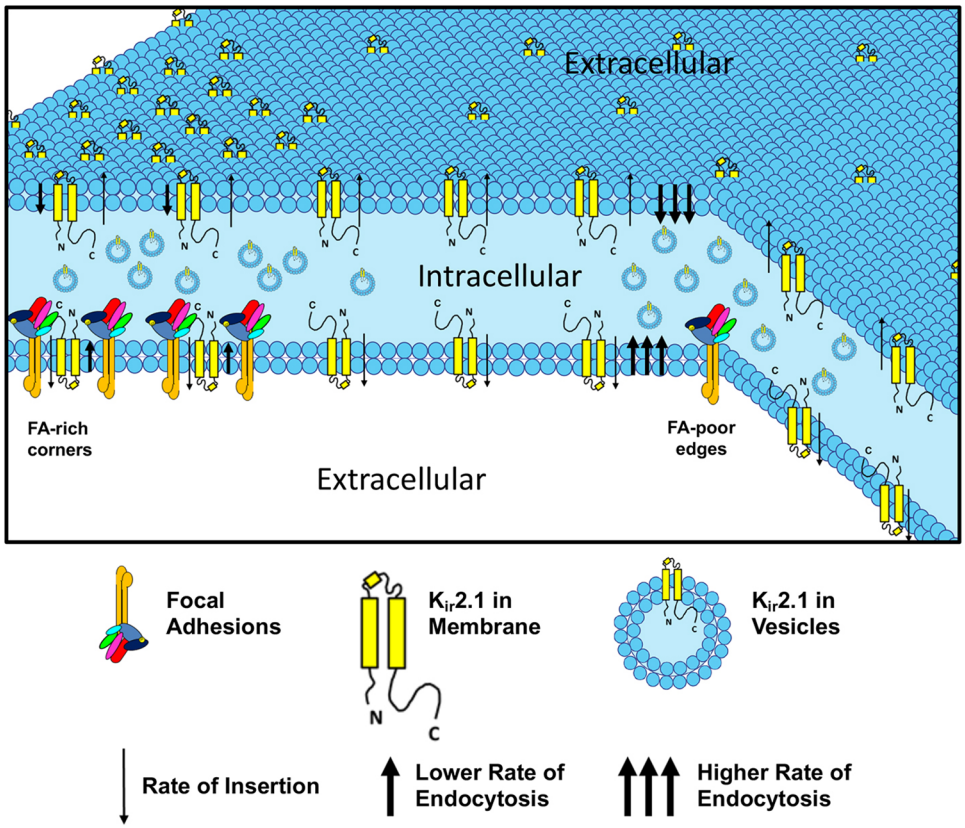

Fig. 7. Proposed mechanism for FA-mediated regulation of $K_{ir}2.1$ localization in cell membrane. Schematic showing a star-shaped cell where the same rate of insertion of $K_{ir}2.1$ to the membrane at corners and edges in conjunction with a faster rate of endocytosis at edges, containing less FAs, and slower rate of endocytosis at corners, containing more FAs, result in a heterogeneous membrane distribution of $K_{ir}2.1$ and I_{K1}.

flow to endothelial cells has been shown to increase $K_{ir}2.1$ channel current in a tyrosine kinase-dependent manner (Hoger et al., 2002), suggesting indirect mechanosensitivity of the channel to shear stress. Notably, the application of shear stress also induces integrin engagement and FA assembly (Jalali et al., 2001). Although our studies were performed in static conditions, I_{K1} amplitude and $K_{ir}2.1$ localization and distribution in membrane were responsive to a variety of intracellular and extracellular modifications of the cytoskeletal mechanics and membrane tension that altered FA coverage and distribution. Specifically, in contrast to the lack of immediate response (Ji et al., 1998), 4 h of hypo-osmotic shock in micropatterned cells resulted in an enhanced FA assembly and a concordant I_{K1} increase. Thus, our results provide evidence for $K_{ir}2.1$ being an indirectly mechanoresponsive channel via known links between mechanical forces and FA dynamics coupled with apparent roles of integrin engagement and FA assembly in $K_{ir}2.1$ endocytosis.

Of significance are also potential implications of our findings for the normal heart development, where a 20–40-fold increase in cardiomyocyte volume (Anversa et al., 1980) and membrane area (Wahler, 1992) is associated with not only a large increase in total I_{K1}, but also a 2.5-fold increased I_{K1} density (Wahler, 1992). Our experiments using monoclonal cell lines and primary cardiomyocytes suggest that increased cardiomyocyte size and associated integrin recruitment may be a contributing factor to the increased I_{K1} density, independent of changes in $K_{ir}2.1$ gene expression. Moreover, ECM in the developing ventricles changes from being primarily fibronectin-based to being laminin-based (Hirschy et al., 2006; Farhadian et al., 1996), which, from our studies, may further contribute to the age-dependent increase in I_{K1}. These considerations may also suggest strategies to augment a low I_{K1} amplitude in pluripotent stem cell-derived cardiomyocytes (Casini et al., 2017). Finally, various cardiac diseases, such as myocardial infarction (Arslan et al., 2011) or pressure overload (Li et al., 2014), are characterized by excess deposition of fibronectin, collagen I and collagen III, and the reduction of laminin as well as reduced I_{K1} density (Nattel et al., 2007), which, based on our studies, could be related to an ECM-dependent reduction in FA coverage and integrin engagement. In general, our results suggest important roles for integrin-modulating signals in I_{K1}-mediated regulation of cell excitability, AP shape and propagation.

Overall, our studies are consistent with a working model (Fig. 7) where engaged integrins are an important contributor to the membrane localization of $K_{ir}2.1$ channels via the local inhibition of dynamin-dependent endocytosis of $K_{ir}2.1$. This mechanism renders the I_{K1} and cellular electrophysiology indirectly mechanosensitive to various intracellular and extracellular signals affecting FA dynamics. These findings warrant future in-depth studies of how cell–matrix interactions modulate the function of various ion channels across diverse cell types and pathophysiological conditions.

MATERIALS AND METHODS

Preparation of micropatterned substrates for cell culture

Cells were micropatterned into circular, square and four-armed star shapes in two sizes, 961 μm^2 and 1600 μm^2, using microcontact printing (Pedrotty et al., 2008; McSpadden et al., 2012). Micropatterns were drawn using AutoCAD (Autodesk, San Rafael, CA) and printed as high-resolution photomasks (chrome on soda-lime; Advance Reproductions, North Andover, MA). Standard soft lithography techniques were used to prepare master micropatterned silicon wafers, as previously described (McSpadden et al., 2012; Pedrotty et al., 2008). Briefly, a silicon wafer (WaferWorld, West Palm Beach, FL) was coated with a 5 µm layer of photoresist (SU8-5; Microchem, Newton, MA), covered with photomask, illuminated with UV light, and washed to remove un-crosslinked photoresist to generate

microfabricated patterns. Poly-dimethylsiloxane (PDMS, Sylgard 184; Dow Corning, Midland, MI) stamps were cast against the microfabricated wafers at 80°C for 2 h, cleaned in 70% ethanol, coated with fibronectin (30 µg/ml in PBS) or laminin (30 µg/ml in PBS) for 1 h, and blow-dried with N_2. The fibronectin micropattern was microcontact-printed from the PDMS stamps onto UV-ozone-treated PDMS-coated 12 mm glass coverslips for 1 h to allow protein transfer. For live-cell imaging, cells were patterned on plasma-treated glass bottom dishes (Fluoro 35 mm, Ibidi, Madison, WI).

Cell culture

Engineered cell lines

For the patch clamp experiments and FA quantification, we utilized the previously described and characterized Ex293 cell line (Kirkton and Bursac, 2011), a monoclonally-derived HEK293 cell line engineered to stably express $K_{ir}2.1$, $Na_v1.5$ and Cx43. In this line, the I_{K1} resulting from exogenously overexpressed $K_{ir}2.1$ was much larger compared to a negligible endogenous I_{K1} present in wild-type HEK293 cells (Kirkton and Bursac, 2011). For live imaging analysis, we used a monoclonal HEK293 line expressing $K_{ir}2.1$ fused to tdTomato at the C-terminus of the channel ($K_{ir}2.1$–tdTomato). In some studies, these cells were also transfected with EGFP fused to the C-terminus of paxillin (paxillin–EGFP, Addgene 15233; Laukaitis et al., 2001). HEK293 cells were maintained in low-glucose DMEM with L-glutamine and sodium pyruvate (11885-092, Gibco, Waltham, MA) supplemented with 10% fetal bovine serum (HyClone, Logan, UT) and 1% penicillin-streptomycin (15140122, Gibco, Waltham, MA). For each experiment, cells were plated onto micropatterned glass coverslips at 10,000 cells per cm^2 and studied within 6–10 h of culture.

Neonatal rat ventricular myocytes

All studies conformed to the Guide for the Care and Use of Laboratory Animals, published by the United States National Institutes of Health (Publication No. 85-23, revised 1996) and approved by Duke University Protocol A214-09-07. NRVMs were isolated from 2-day-old Sprague Dawley rats, as previously described (Badie and Bursac, 2009; McSpadden et al., 2012; Jackman et al., 2016) using overnight digestion in 0.1% trypsin and four serial dissociations with 0.1% collagenase. The obtained cell suspension was pre-plated on a tissue culture flask for 45 min to enrich the fraction of cardiomyocytes. Non-adherent cells were collected, centrifuged, re-suspended, counted and plated onto micropatterned fibronectin substrates at density of 40,000 cells/cm^2 in DMEM/F-12 (11330-057, Gibco) supplemented with 10% fetal bovine serum, 10% horse serum, penicillin (5 U/ml) and vitamin B12 (2 µg/ml). After 24 h, the cell culture medium was changed to DMEM/F12 supplemented with 2% fetal bovine serum, penicillin and vitamin B12. All experiments were performed after 3–4 days of culture.

Whole-cell and cell-attached membrane current recordings

Glass coverslips with micropatterned cells were transferred to a patch-clamp chamber perfused with Tyrode's solution containing (in mM): 135 NaCl, 5.4 KCl, 1.8 $CaCl_2$, 1 $MgCl_2$, 0.33 NaH_2PO_4, 5 HEPES and 5 glucose. Patch pipettes were fabricated with tip resistances of 1–2 MΩ when filled with pipette solution consisting of (in mM): 140 KCl, 10 NaCl, 1 $CaCl_2$, 2 $MgCl_2$, 10 EGTA, 10 HEPES and 5 MgATP. Whole-cell voltage-clamp recordings were acquired at room temperature (25°C), using the Multiclamp 700B amplifier (Axon Instruments), filtered with a 10-kHz Bessel filter, digitized at 40 kHz and analyzed using WinWCP software (John Dempster, University of Strathclyde). A steady-state I_{K1}–V curve was constructed from the current responses to 1 s test potentials (−130 to 50 mV, increments of 10 mV) from a holding potential of −40 mV (McSpadden et al., 2012; Nguyen et al., 2016). A steady-state I_{Na}–V curve was constructed from the peak current responses to various 500 ms test potentials (−60 to 60 mV, increments of 10 mV) from a holding potential of −80 mV (Kirkton and Bursac, 2011). APs were elicited by injecting a 1 ms current pulse at 1.1× threshold amplitude.

For cell-attached membrane current recordings, patch electrodes were fabricated with tip resistances of 5.0–10.0 MΩ (for HEK293 cells) and 1.5–3.0 MΩ (for NRVMs) when filled with pipette solution consisting of (in mM): 140 KCl, 1 $CaCl_2$, and 5 HEPES. Bath solution consisted of (in mM): 140 KCl, 1.8 $CaCl_2$, 5 HEPES, and 0.33 NaH_2PO_4. I_{K1} currents were recorded using a similar protocol, filtered with a 2-kHz Bessel filter, digitized at 40 kHz and analyzed using WinWCP software, as previously described (Vaidyanathan et al., 2010).

Immunostaining and imaging

Micropatterned cells on coverslips were fixed in 4% paraformaldehyde (PFA) for 5 min and permeabilized with 0.1% (v/v) Triton-X at room temperature (10 min for HEK293 cells, 30 min for NRVMs). Primary antibodies were diluted in blocking solution (5:1 solution of 1% BSA and chicken serum) and applied overnight at 4°C and included: anti-Vinculin (1:800, mouse monoclonal, V9131, Sigma), anti-Paxillin (1:300, rabbit monoclonal, ab32084, Abcam), anti-talin (1:300, mouse monoclonal, T3287, Sigma), anti-active β1-integrin (1:300, mouse monoclonal, ab30394, Abcam), anti-$Na_v1.5$ (1:100, rabbit monoclonal, ASC-005, Alomone) and anti-Cx43 (1:300, rabbit monoclonal, ab11370, Abcam) antibodies. The secondary antibodies were conjugated to Alexa Fluor 488 (1:300, chicken anti-rabbit-IgG, Life Technologies) or Alexa Fluor 594 (1:300, chicken anti-mouse-IgG, Life Technologies) and were applied for 1 h at room temperature. Nuclei were counterstained with DAPI (1:250, Sigma). Alexa Fluor 488–phalloidin (1:150, Thermo Fisher Scientific) was used to visualize actin fibers in cardiomyocytes. Cell Mask Green Plasma Membrane Stain (1:1000, Thermo Fisher Scientific) was used to visualize cell membrane in HEK293 cells.

Adult rat left ventricles were excised from 3-month-old female Sprague Dawley rats, rinsed in 30% sucrose solution followed by PBS, embedded in Tissue-Tek O.C.T. Compound (Sakura Finetek), snap-frozen in liquid nitrogen and placed at −80°C overnight. Samples were then cryosectioned at 5 µm thickness, brought to room temperature, briefly rehydrated, then fixed in 4% PFA for 10 mins and permeabilized overnight at 4°C in a solution containing 0.5% (v/v) Triton-X, 1% (w/v) BSA and 10% (v/v) chicken serum. Primary antibodies were diluted in blocking solution [0.5% (v/v) Triton-X, 1% (w/v) BSA and 3% (v/v) chicken serum] and applied overnight at 4°C and included: anti-$K_{ir}2.1$(1:100, rabbit monoclonal, ASC-026, Alomone) and anti-β1D integrin (1:200, mouse monoclonal, MAB1900, EMD Millipore) antibodies. The secondary antibodies included Alexa Fluor 488 (1:300, chicken anti-rabbit-IgG, Life Technologies) and Alexa Fluor 594 (1:300, chicken anti-mouse-IgG, Life Technologies) and were applied for 1 h at room temperature.

All samples were imaged at 40× magnification (HCX PL APO 40×/NA1.25 oil objective; Leica Microsystems, Buffalo Grove, IL), 4× optical zoom, and a pinhole size of 1 Airy Unit (~1.2 µm slice thickness) using an inverted confocal microscope (Leica, DMI6000CS) and Leica LAS AF 2.6 imaging software. The full width at half maximum of the point spread function was ~290 nm for the 488 nm excitation wavelength and ~310 nm for the 561 nm excitation wavelength. Live cells were imaged using the same system, while being maintained at 37°C.

Image analysis

Micropatterned cells stained for vinculin, paxillin, talin or active β1-integrin, as well as live cells containing $K_{ir}2.1$–tdTomato and EGFP–paxillin, were imaged by confocal microscopy in the plane of the cell–substrate interface and analyzed using custom ImageJ macros (available from the corresponding author upon request). Masks were created for each analyzed cell by increasing contrast to identify the cell boundaries. To facilitate the visualization of the cell periphery, sub-masks were created at 80% of the cell boundary and the interior pixels within the sub-mask were removed. Images were then cropped to a tightest square image containing the cell and pixel values from different cells of same shape and size were summed into a stack image and pseudocolored to create heatmaps (Gomez and Nelson, 2011). In heatmaps, the removed interior pixels from the sub-masks were marked in black.

For the quantification of FA coverage, FAs were segmented using the 'water' algorithm, as previously described (Rothenberg et al., 2015; Zamir et al., 1999). The sums of the areas of all segmented FAs were reported as total FA coverage (in μm^2). For integrin staining, structures smaller than 0.5 μm^2 were excluded. Furthermore, integrin immunostaining yielded significant nuclear staining that did not contain identifiable FA structures;

therefore, DAPI-stained images were thresholded and converted into binary masks, which were applied to images of stained integrin to remove nuclear integrin signal. For all FA images in micropatterned Ex293 cells, the pixel size was 0.0183 μm^2.

Local FA coverage in micropatterned cells was quantified (in μm^2) by the same water method as mentioned above, followed by dividing each cell into a 5×5 grid resulting in 25 regions (Fig. S6A–C). Four of these regions were denoted as 'corners' and four other regions were denoted as 'edges' depending on the shape of the cell. The FA-positive areas of pixels in the corner and edge regions were calculated. The mean FA area averaged over four corners or four edges was termed the 'local' FA coverage. Similar methods were used to measure the mean intensities of $K_{ir}2.1$–tdTomato and CellMask Green at cell corners and edges.

Immunostained sections of adult rat ventricles were used to quantify spatial relationships between $K_{ir}2.1$ channels (stained in green) and β1D integrins (stained in red). Each analyzed cardiomyocyte was divided into multiple 't-tubule regions' in the cell interior and 'costamere regions' at the lateral cell boundaries (Fig. 6K). Custom ImageJ macros (available from the corresponding author upon request) allowed the user to select lines within these regions along which fluorescence intensity profiles were measured in the green and red channels. These lines were selected to encompass the two fluorophores and to be orthogonal to either the registered t-tubule pattern (along the longitudinal cell axis) or lateral membrane (along the transverse cell axis) (Fig. 6L). From the obtained intensity profiles, a custom MATLAB script (available from the corresponding author upon request) then calculated the closest distance between the green and red fluorescence peaks (Fig. 6M).

Microsphere assay

Polystyrene microsphere beads (10 µm diameter; Polysciences, Inc., Warrington, PA) were washed three times in PBS and incubated in 0.1% (w/v) poly-L-Lysine(Sigma), or 500 µg/ml fibronectin for 1 h at 37°C. Microspheres were then washed in PBS and added (10^6 beads per cm^2) onto $K_{ir}2.1$–tdTomato-expressing HEK293 cells already spread on a fibronectin-coated plate. After 4 h, cell membranes were stained with CellMask Green, and imaged at the bead plane within the next hour using a confocal microscope. The mean intensities of CellMask Green and $K_{ir}2.1$–tdTomato around a bead were quantified and their ratio was reported as a measure of the channel density at the membrane.

Surface biotinylation assay

The surface biotinylation assay was performed following previously described methods (Li et al., 2016). Specifically, cells were plated in 10-cm tissue culture-treated dishes at 800,000 cells/dish and FAK inhibitor was added 2 h after plating. At 6 h after treatment, medium was replaced with ice-cold DMEM containing 30 mM HEPES (pH 7.4) for 10 min. The biotin solution was prepared freshly by dissolving EZ-LinkSulfo-NHS-SS Biotin (Pierce) at 0.5 mg/ml in cold HBSS (Gibco) with Ca^{2+} and Mg^{2+} and added to the cells. The biotinylation reaction was performed at 4°C for 30 min with gentle end-over-end mixing. The reaction was terminated by washing the cells three times with ice-cold HBSS (with Ca^{2+} and Mg^{2+}) containing 20 mM glycine. Cells were lysed in lysis buffer (RIPA buffer, 20 mM glycine, and complete protease inhibitor) and centrifuged at 12,000 ***g*** for 10 min. Protein concentration was measured via a BCA assay (Pierce). 700 µg of protein from each sample was incubated with streptavidin microspheres (Pierce) overnight at 4°C. Microspheres were washed four times with lysis buffer and the streptavidin-bound biotinylated proteins were eluted and resolved by SDS-PAGE followed by western blotting.

Western blotting

Protein extracts were assessed by western blot analysis, as described in our previous studies (Jackman et al., 2016). Briefly, 20 µg of each protein sample was loaded in each lane of a 10% polyacrylamide gel and transferred onto a PVDF membrane. The membrane was then blocked in TBS with 0.05% Tween 20 and 5% milk. To detect $K_{ir}2.1$ protein level, anti-Kir2.1 antibody (1:200, ASC-026, Alomone Labs, rabbit monoclonal) was diluted in TBS with 0.05% Tween 20 and 3% BSA (4°C, overnight). As the internal reference, tubulin were blotted by using anti-tubulin antibody (1:10,000, ab6046, Abcam). HRP-conjugated secondary antibodies were applied for 1 h at room temperature. Chemiluminescence was imaged using a Bio-Rad ChemiDoc system and protein levels were quantified by ImageJ.

Inhibitors, activators, and reagents

$Mn(II)Cl_2$ (1 mM, Sigma), FAK-Inhibitor PF-573228 (100 µM, Tocris) and Blebbistatin (10 µM, Stem Cell Technologies) were used to modulate FA assembly. Nocodazole (12 µM, Sigma) and Dynasore (25 µM, Sigma) were used to inhibit forward and reverse trafficking of $K_{ir}2.1$. For Dynasore experiments, FBS in the culture medium was replaced with NuSerum (Thermo Fisher Scientific, Pittsburgh, PA). For all experiments, cells were exposed to drugs for 2, 4 or 6 h prior to patch clamp recordings and immunostaining. These short exposure times were selected to avoid major changes in $K_{ir}2.1$ gene or protein expression. For the vehicle control group (VC), cells were exposed to the vehicle solution alone (no drug) for 6 h.

FRAP

HEK293 cells expressing $K_{ir}2.1$–tdTomato were patterned into star shapes. Samples were imaged as previously described (Rothenberg et al., 2018) with a 60× magnification objective (UPlanSApo 60×/NA 1.35 Objective; Olympus, Tokyo, Japan) on an inverted fluorescent microscope (Olympus IX83) illuminated by a xenon arc lamp (Lambda LS) equipped with a 300 W ozone-free xenon bulb (Sutter Instrument, Novato, CA). The images were captured using a sCMOS ORCA-Flash4.0 V2 camera (Hamamatsu Photonics, Hamamatsu, Japan). User-defined regions of interest (ROI) were photobleached using a 515 nm laser (FRAPPA; Andor Technology, Belfast, UK). Fixed cells were used to create a bleaching protocol (10 laser pulses with a dwell time of 1000 µs per pixel) that resulted in 80% reduction in fluorescence intensity in control cells. This threshold was chosen to allow for significant fluorescent recovery, but minimize the chances of photo-damage. As has been observed in previous studies (Canel et al., 2010; Jaskolski et al., 2009), Dynasore treatment reduced the bleaching efficiency. Therefore, the mobile fraction was calculated to explicitly account for this variation in bleaching efficiency.

Pre- and post-photobleaching images of patterned live cells were acquired every 10 s until 5 min after photobleaching using custom filter set comprising a TRITC excitation filter (FF01-560/25; Semrock, Rochester, NY), RFP emission filter (FF01-607/36; Semrock, Rochester, NY) and dichroic mirror (FF410/504/582/669-Di01; Semrock, Rochester, NY). The motorized filter wheels (Lambda 10-3; Sutter Instrument) and automated stage (H117EIX3; Prior Scientific, Rockland, MA), as well as photobleaching and image acquisition were controlled through MetaMorph Advanced software (Olympus).

FRAP analysis

User-defined polygons were used to outline a non-cellular background region outside of the cells, the bleached region of a corner, the bleached region of an edge and an unbleached region of the cell. To calculate the normalized recovery, the intensity of the background region was first subtracted from pixel intensities within cell. To account for global bleaching, the mean intensity of the background-subtracted bleached membrane regions was divided by the mean intensity of the background-subtracted unbleached region from the same cell. Finally, to normalize the pre-bleach intensity to one, the curves were divided by the average value of the background-subtracted and bleaching-corrected recovery curve from the pre-bleaching time points. Each normalized recovery curve was fit to a single exponential recovery equation:

$$\text{Normalized FRAP} = R_o + (R_f - R_o)(1 - e^{-(t/\tau)}) \quad (1)$$

where R_f is the final recovery, R_o is the initial recovery and τ is the time constant of recovery. τ values were averaged over different cells and reported. The mobile fraction, M_f, was calculated using Eqn 2 (Kang et al., 2012) for each cell, then averaged, and reported:

$$M_f = \frac{R_f - R_o}{1 - R_O} \quad (2)$$

Statistical analysis

Data are presented as mean±s.e.m. and were evaluated for statistical significance using a Student's *t*-test or an analysis of variance (one-way, α-factor of 0.05) followed by Dunnett's post hoc test. When appropriate, an analysis of variance (two-way, α-factor of 0.05) followed by Tukey's post hoc test for multiple comparisons was used. Differences between groups were considered statistically significance for $P<0.05$.

Acknowledgements

We acknowledge H. Nguyen, C. Jackman, R. Gorsuch and I. Puranam for technical support and critical discussions of the manuscript.

Competing interests

The authors declare no competing or financial interests.

Author contributions

Conceptualization: S.S., B.D.H., N.B.; Methodology: S.S.; Software: S.S., K.E.R.; Validation: S.S., K.E.R.; Formal analysis: S.S., K.E.R.; Investigation: S.S., H.L.; Resources: S.S.; Data curation: S.S.; Writing - original draft: S.S.; Writing - review & editing: S.S., B.D.H., N.B.; Visualization: S.S.; Supervision: B.D.H., N.B.; Project administration: S.S.; Funding acquisition: N.B.

Funding

This study was supported by National Institutes of Health grants 1R01HL126524, 1R01HL132389 and U01HL134764 (to N.B.), a National Science Foundation CAREER award (to B.D.H.), and National Science Foundation Graduate Research Fellowships (to S.S. and K.E.R.). Deposited in PMC for release after 12 months.

Supplementary information

Supplementary information available online at
http://jcs.biologists.org/lookup/doi/10.1242/jcs.225383.supplemental

References

Alanko, J., Mai, A., Jacquemet, G., Schauer, K., Kaukonen, R., Saari, M., Goud, B. and Ivaska, J. (2015). Integrin endosomal signalling suppresses anoikis. *Nat. Cell Biol.* **17**, 1412-1421. doi:10.1038/ncb3250

Anversa, P., Olivetti, G. and Loud, A. V. (1980). Morphometric study of early postnatal development in the left and right ventricular myocardium of the rat. I. Hypertrophy, hyperplasia, and binucleation of myocytes. *Circ. Res.* **46**, 495-502. doi:10.1161/01.RES.46.4.495

Arcangeli, A. and Becchetti, A. (2006). Complex functional interaction between integrin receptors and ion channels. *Trends Cell Biol.* **16**, 631-639. doi:10.1016/j.tcb.2006.10.003

Arslan, F., Smeets, M. B., Riem Vis, P. W., Karper, J. C., Quax, P. H., Bongartz, L. G., Peters, J. H., Hoefer, I. E., Doevendans, P. A., Pasterkamp, G. et al. (2011). Lack of fibronectin-EDA promotes survival and prevents adverse remodeling and heart function deterioration after myocardial infarction. *Circ. Res.* **108**, 582-592. doi:10.1161/CIRCRESAHA.110.224428

Badie, N. and Bursac, N. (2009). Novel micropatterned cardiac cell cultures with realistic ventricular microstructure. *Biophys. J.* **96**, 3873-3885. doi:10.1016/j.bpj.2009.02.019

Balse, E. and Boycott, H. E. (2017). Ion channel trafficking: control of ion channel density as a target for arrhythmias? *Front. Physiol.* **8**, 808. doi:10.3389/fphys.2017.00808

Balse, E., Steele, D. F., Abriel, H., Coulombe, A., Fedida, D. and Hatem, S. N. (2012). Dynamic of ion channel expression at the plasma membrane of cardiomyocytes. *Physiol. Rev.* **92**, 1317-1358. doi:10.1152/physrev.00041.2011

Bates, E. (2015). Ion channels in development and cancer. *Annu. Rev. Cell Dev. Biol.* **31**, 231-247. doi:10.1146/annurev-cellbio-100814-125338

Bazzoni, G., Shih, D.-T., Buck, C. A. and Hemler, M. E. (1995). Monoclonal antibody 9EG7 defines a novel beta 1 integrin epitope induced by soluble ligand and manganese, but inhibited by calcium. *J. Biol. Chem.* **270**, 25570-25577. doi:10.1074/jbc.270.43.25570

Becchetti, A., Pillozzi, S., Morini, R., Nesti, E. and Arcangeli, A. (2010). New insights into the regulation of ion channels by integrins. *Int. Rev. Cell Mol. Biol.* **279**, 135-190. doi:10.1016/S1937-6448(10)79005-5

Bendahhou, S., Donaldson, M. R., Plaster, N. M., Tristani-Firouzi, M., Fu, Y.-H. and Ptácek, L. J. (2003). Defective potassium channel Kir2.1 trafficking underlies Andersen-Tawil syndrome. *J. Biol. Chem.* **278**, 51779-51785. doi:10.1074/jbc.M310278200

Beuckelmann, D. J., Näbauer, M. and Erdmann, E. (1993). Alterations of K+ currents in isolated human ventricular myocytes from patients with terminal heart failure. *Circ. Res.* **73**, 379-385. doi:10.1161/01.RES.73.2.379

Bottcher, R. T. and Fassler, R. (2014). Membrane tension drives ligand-independent integrin signaling. *EMBO J.* **33**, 2439-2441. doi:10.15252/embj.201489886

Boulant, S., Kural, C., Zeeh, J.-C., Ubelmann, F. and Kirchhausen, T. (2011). Actin dynamics counteract membrane tension during clathrin-mediated endocytosis. *Nat. Cell Biol.* **13**, 1124-1131. doi:10.1038/ncb2307

Boycott, H. E., Barbier, C. S. M., Eichel, C. A., Costa, K. D., Martins, R. P., Louault, F., Dilanian, G., Coulombe, A., Hatem, S. N. and Balse, E. (2013). Shear stress triggers insertion of voltage-gated potassium channels from intracellular compartments in atrial myocytes. *Proc. Natl. Acad. Sci. USA* **110**, E3955-E3964. doi:10.1073/pnas.1309896110

Bridgewater, R. E., Norman, J. C. and Caswell, P. T. (2012). Integrin trafficking at a glance. *J. Cell Sci.* **125**, 3695-3701. doi:10.1242/jcs.095810

Burridge, K., Chrzanowska-Wodnicka, M. and Zhong, C. (1997). Focal adhesion assembly. *Trends Cell Biol.* **7**, 342-347. doi:10.1016/S0962-8924(97)01127-6

Canel, M., Serrels, A., Anderson, K. I., Frame, M. C. and Brunton, V. G. (2010). Use of photoactivation and photobleaching to monitor the dynamic regulation of E-cadherin at the plasma membrane. *Cell Adh. Migr.* **4**, 491-501. doi:10.4161/cam.4.4.12661

Casini, S., Verkerk, A. O. and Remme, C. A. (2017). Human iPSC-derived cardiomyocytes for investigation of disease mechanisms and therapeutic strategies in inherited arrhythmia syndromes: strengths and limitations. *Cardiovasc. Drugs Ther.* **31**, 325-344. doi:10.1007/s10557-017-6735-0

Chen, C. S., Alonso, J. L., Ostuni, E., Whitesides, G. M. and Ingber, D. E. (2003). Cell shape provides global control of focal adhesion assembly. *Biochem. Biophys. Res. Commun.* **307**, 355-361. doi:10.1016/S0006-291X(03)01165-3

Chittajallu, R., Chen, Y., Wang, H., Yuan, X., Ghiani, C. A., Heckman, T., Mcbain, C. J. and Gallo, V. (2002). Regulation of Kv1 subunit expression in oligodendrocyte progenitor cells and their role in G1/S phase progression of the cell cycle. *Proc. Natl. Acad. Sci. USA* **99**, 2350-2355. doi:10.1073/pnas.042698399

Clark, R. B., Tremblay, A., Melnyk, P., Allen, B. G., Giles, W. R. and Fiset, C. (2001). T-tubule localization of the inward-rectifier K(+) channel in mouse ventricular myocytes: a role in K(+) accumulation. *J. Physiol.* **537**, 979-992. doi:10.1113/jphysiol.2001.012708

Davis, M. J., Wu, X., Nurkiewicz, T. R., Kawasaki, J., Gui, P., Hill, M. A. and Wilson, E. (2002). Regulation of ion channels by integrins. *Cell Biochem. Biophys.* **36**, 41-66. doi:10.1385/CBB:36:1:41

Enomoto, T. (1996). Microtubule disruption induces the formation of actin stress fibers and focal adhesions in cultured cells: possible involvement of the rho signal cascade. *Cell Struct. Funct.* **21**, 317-326. doi:10.1247/csf.21.317

Faelber, K., Held, M., Gao, S., Posor, Y., Haucke, V., Noé, F. and Daumke, O. (2012). Structural insights into dynamin-mediated membrane fission. *Structure* **20**, 1621-1628. doi:10.1016/j.str.2012.08.028

Farhadian, F., Contard, F., Sabri, A., Samuel, J. L. and Rappaport, L. (1996). Fibronectin and basement membrane in cardiovascular organogenesis and disease pathogenesis. *Cardiovasc. Res.* **32**, 433-442. doi:10.1016/S0008-6363(96)00119-8

Ferguson, J. P., Huber, S. D., Willy, N. M., Aygün, E., Goker, S., Atabey, T. and Kural, C. (2017). Mechanoregulation of clathrin-mediated endocytosis. *J. Cell Sci.* **130**, 3631-3636. doi:10.1242/jcs.205930

Friedland, J. C., Lee, M. H. and Boettiger, D. (2009). Mechanically activated integrin switch controls alpha5beta1 function. *Science* **323**, 642-644. doi:10.1126/science.1168441

Gautrot, J. E., Malmström, J., Sundh, M., Margadant, C., Sonnenberg, A. and Sutherland, D. S. (2014). The nanoscale geometrical maturation of focal adhesions controls stem cell differentiation and mechanotransduction. *Nano Lett.* **14**, 3945-3952. doi:10.1021/nl501248y

Geiger, B. and Yamada, K. M. (2011). Molecular architecture and function of matrix adhesions. *Cold Spring Harb. Perspect. Biol.* **3**, a005033. doi:10.1101/cshperspect.a005033

Geiger, B., Spatz, J. P. and Bershadsky, A. D. (2009). Environmental sensing through focal adhesions. *Nat. Rev. Mol. Cell Biol.* **10**, 21-33. doi:10.1038/nrm2593

Gomez, E. W. and Nelson, C. M. (2011). Lithographically defined two- and three-dimensional tissue microarrays. In *Biological Microarrays: Methods and Protocols* (ed. A. Khademhosseini, K.-Y. Suh and M. Zourob), pp 107-116. Totowa, NJ: Humana Press.

Grosberg, A., Kuo, P.-L., Guo, C.-L., Geisse, N. A., Bray, M.-A., Adams, W. J., Sheehy, S. P. and Parker, K. K. (2011). Self-organization of muscle cell structure and function. *PLoS Comput. Biol.* **7**, e1001088. doi:10.1371/journal.pcbi.1001088

Hansen, C. G. and Nichols, B. J. (2009). Molecular mechanisms of clathrin-independent endocytosis. *J. Cell Sci.* **122**, 1713-1721. doi:10.1242/jcs.033951

Hibino, H., Inanobe, A., Furutani, K., Murakami, S., Findlay, I. and Kurachi, Y. (2010). Inwardly rectifying potassium channels: their structure, function, and physiological roles. *Physiol. Rev.* **90**, 291-366. doi:10.1152/physrev.00021.2009

Hirakawa, M., Oike, M., Karashima, Y. and Ito, Y. (2004). Sequential activation of RhoA and FAK/paxillin leads to ATP release and actin reorganization in human endothelium. *J. Physiol.* **558**, 479-488. doi:10.1113/jphysiol.2004.065334

Hirschy, A., Schatzmann, F., Ehler, E. and Perriard, J.-C. (2006). Establishment of cardiac cytoarchitecture in the developing mouse heart. *Dev. Biol.* **289**, 430-441. doi:10.1016/j.ydbio.2005.10.046

Hoffman, B. D., Grashoff, C. and Schwartz, M. A. (2011). Dynamic molecular processes mediate cellular mechanotransduction. *Nature* **475**, 316-323. doi:10.1038/nature10316

Hofherr, A., Fakler, B. and Klocker, N. (2005). Selective Golgi export of Kir2.1 controls the stoichiometry of functional Kir2.x channel heteromers. *J. Cell Sci.* **118**, 1935-1943. doi:10.1242/jcs.02322

Hoger, J. H., Ilyin, V. I., Forsyth, S. and Hoger, A. (2002). Shear stress regulates the endothelial Kir2.1 ion channel. *Proc. Natl. Acad. Sci. USA* **99**, 7780-7785. doi:10.1073/pnas.102184999

Huynh, T. V., Chen, F., Wetzel, G. T., Friedman, W. F. and Klitzner, T. S. (1992). Developmental changes in membrane Ca2+ and K+ currents in fetal, neonatal, and adult rabbit ventricular myocytes. *Circ. Res.* **70**, 508-515. doi:10.1161/01.RES.70.3.508

Israeli-Rosenberg, S., Chen, C., Li, R., Deussen, D. N., Niesman, I. R., Okada, H., Patel, H. H., Roth, D. M. and Ross, R. S. (2015). Caveolin modulates integrin function and mechanical activation in the cardiomyocyte. *FASEB J.* **29**, 374-384. doi:10.1096/fj.13-243139

Jackman, C. P., Carlson, A. L. and Bursac, N. (2016). Dynamic culture yields engineered myocardium with near-adult functional output. *Biomaterials* **111**, 66-79. doi:10.1016/j.biomaterials.2016.09.024

Jacot, J. G., Martin, J. C. and Hunt, D. L. (2010). Mechanobiology of cardiomyocyte development. *J. Biomech.* **43**, 93-98. doi:10.1016/j.jbiomech.2009.09.014

Jalali, S., del Pozo, M. A., Chen, K.-D., Miao, H., Li, Y.-S., Schwartz, M. A., Shyy, J. Y.-J. and Chien, S. (2001). Integrin-mediated mechanotransduction requires its dynamic interaction with specific extracellular matrix (ECM) ligands. *Proc. Natl. Acad. Sci. USA* **98**, 1042-1046. doi:10.1073/pnas.98.3.1042

Jaskolski, F., Mayo-Martin, B., Jane, D. and Henley, J. M. (2009). Dynamin-dependent membrane drift recruits AMPA receptors to dendritic spines. *J. Biol. Chem.* **284**, 12491-12503. doi:10.1074/jbc.M808401200

Ji, S., John, S. A., Lu, Y. and Weiss, J. N. (1998). Mechanosensitivity of the cardiac muscarinic potassium channel. A novel property conferred by Kir3.4 subunit. *J. Biol. Chem.* **273**, 1324-1328. doi:10.1074/jbc.273.3.1324

Kanchanawong, P., Shtengel, G., Pasapera, A. M., Ramko, E. B., Davidson, M. W., Hess, H. F. and Waterman, C. M. (2010). Nanoscale architecture of integrin-based cell adhesions. *Nature* **468**, 580-584. doi:10.1038/nature09621

Kang, M., Day, C. A., Kenworthy, A. K. and Dibenedetto, E. (2012). Simplified equation to extract diffusion coefficients from confocal FRAP data. *Traffic* **13**, 1589-1600. doi:10.1111/tra.12008

Kilian, K. A., Bugarija, B., Lahn, B. T. and Mrksich, M. (2010). Geometric cues for directing the differentiation of mesenchymal stem cells. *Proc. Natl. Acad. Sci. USA* **107**, 4872-4877. doi:10.1073/pnas.0903269107

Kirkton, R. D. and Bursac, N. (2011). Engineering biosynthetic excitable tissues from unexcitable cells for electrophysiological and cell therapy studies. *Nat. Commun.* **2**, 300. doi:10.1038/ncomms1302

Kléber, A. G. and Rudy, Y. (2004). Basic mechanisms of cardiac impulse propagation and associated arrhythmias. *Physiol. Rev.* **84**, 431-488. doi:10.1152/physrev.00025.2003

Kostin, S., Scholz, D., Shimada, T., Maeno, Y., Mollnau, H., Hein, S. and Schaper, J. (1998). The internal and external protein scaffold of the T-tubular system in cardiomyocytes. *Cell Tissue Res.* **294**, 449-460. doi:10.1007/s004410051196

Laukaitis, C. M., Webb, D. J., Donais, K. and Horwitz, A. F. (2001). Differential dynamics of alpha 5 integrin, paxillin, and alpha-actinin during formation and disassembly of adhesions in migrating cells. *J. Cell Biol.* **153**, 1427-1440. doi:10.1083/jcb.153.7.1427

Leonoudakis, D., Conti, L. R., Anderson, S., Radeke, C. M., McGuire, L. M. M., Adams, M. E., Froehner, S. C., Yates, J. R., III and Vandenberg, C. A. (2004). Protein trafficking and anchoring complexes revealed by proteomic analysis of inward rectifier potassium channel (Kir2.x)-associated proteins. *J. Biol. Chem.* **279**, 22331-22346. doi:10.1074/jbc.M400285200

Li, A.-H., Liu, P. P., Villarreal, F. J. and Garcia, R. A. (2014). Dynamic changes in myocardial matrix and relevance to disease: translational perspectives. *Circ. Res.* **114**, 916-927. doi:10.1161/CIRCRESAHA.114.302819

Li, H., Spagnol, G., Zheng, L., Stauch, K. L. and Sorgen, P. L. (2016). Regulation of Connexin43 function and expression by tyrosine kinase 2. *J. Biol. Chem.* **291**, 15867-15880. doi:10.1074/jbc.M116.727008

Lin, G. L., Cohen, D. M., Desai, R. A., Breckenridge, M. T., Gao, L., Humphries, M. J. and Chen, C. S. (2013). Activation of beta 1 but not beta 3 integrin increases cell traction forces. *FEBS Lett.* **587**, 763-769. doi:10.1016/j.febslet.2013.01.068

Loewen, M. E., Wang, Z. R., Eldstrom, J., Zadeh, A. D., Khurana, A., Steele, D. F. and Fedida, D. (2009). Shared requirement for dynein function and intact microtubule cytoskeleton for normal surface expression of cardiac potassium channels. *Am. J. Physiol. Heart Circ. Physiol.* **296**, H71-H83. doi:10.1152/ajpheart.00260.2008

Ma, D., Taneja, T. K., Hagen, B. M., Kim, B.-Y., Ortega, B., Lederer, W. J. and Welling, P. A. (2011). Golgi export of the Kir2.1 channel is driven by a trafficking signal located within its tertiary structure. *Cell* **145**, 1102-1115. doi:10.1016/j.cell.2011.06.007

Macia, E., Ehrlich, M., Massol, R., Boucrot, E., Brunner, C. and Kirchhausen, T. (2006). Dynasore, a cell-permeable inhibitor of dynamin. *Dev. Cell* **10**, 839-850. doi:10.1016/j.devcel.2006.04.002

Mandal, K., Wang, I., Vitiello, E., Orellana, L. A. C. and Balland, M. (2014). Cell dipole behaviour revealed by ECM sub-cellular geometry. *Nat. Commun.* **5**, 5749. doi:10.1038/ncomms6749

Mcspadden, L. C., Kirkton, R. D. and Bursac, N. (2009). Electrotonic loading of anisotropic cardiac monolayers by unexcitable cells depends on connexin type and expression level. *Am. J. Physiol. Cell Physiol.* **297**, C339-C351. doi:10.1152/ajpcell.00024.2009

Mcspadden, L. C., Nguyen, H. and Bursac, N. (2012). Size and ionic currents of unexcitable cells coupled to cardiomyocytes distinctly modulate cardiac action potential shape and pacemaking activity in micropatterned cell pairs. *Circ. Arrhythm Electrophysiol.* **5**, 821-830. doi:10.1161/CIRCEP.111.969329

Miake, J., Marbán, E. and Nuss, H. B. (2003). Functional role of inward rectifier current in heart probed by Kir2.1 overexpression and dominant-negative suppression. *J. Clin. Invest.* **111**, 1529-1536. doi:10.1172/JCI200317959

Milstein, M. L., Musa, H., Balbuena, D. P., Anumonwo, J. M. B., Auerbach, D. S., Furspan, P. B., Hou, L., Hu, B., Schumacher, S. M., Vaidyanathan, R. et al. (2012). Dynamic reciprocity of sodium and potassium channel expression in a macromolecular complex controls cardiac excitability and arrhythmia. *Proc. Natl. Acad. Sci. USA* **109**, E2134-E2143. doi:10.1073/pnas.1109370109

Nattel, S., Maguy, A., le Bouter, S. and Yeh, Y.-H. (2007). Arrhythmogenic ion-channel remodeling in the heart: heart failure, myocardial infarction, and atrial fibrillation. *Physiol. Rev.* **87**, 425-456. doi:10.1152/physrev.00014.2006

Nguyen, H. X., Kirkton, R. D. and Bursac, N. (2016). Engineering prokaryotic channels for control of mammalian tissue excitability. *Nat. Commun.* **7**, 13132. doi:10.1038/ncomms13132

Noam, Y., Ehrengruber, M. U., Koh, A., Feyen, P., Manders, E. M. M., Abbott, G. W., Wadman, W. J. and Baram, T. Z. (2014). Filamin A promotes dynamin-dependent internalization of hyperpolarization-activated cyclic nucleotide-gated type 1 (HCN1) channels and restricts Ih in hippocampal neurons. *J. Biol. Chem.* **289**, 5889-5903. doi:10.1074/jbc.M113.522060

Okada, H., Lai, N. C., Kawaraguchi, Y., Liao, P., Copps, J., Sugano, Y., Okada-Maeda, S., Banerjee, I., Schilling, J. M., Gingras, A. R. et al. (2013). Integrins protect cardiomyocytes from ischemia/reperfusion injury. *J. Clin. Invest.* **123**, 4294-4308. doi:10.1172/JCI64216

Palazzo, A. F., Eng, C. H., Schlaepfer, D. D., Marcantonio, E. E. and Gundersen, G. G. (2004). Localized stabilization of microtubules by integrin- and FAK-facilitated Rho signaling. *Science* **303**, 836-839. doi:10.1126/science.1091325

Parsons, J. T., Horwitz, A. R. and Schwartz, M. A. (2010). Cell adhesion: integrating cytoskeletal dynamics and cellular tension. *Nat. Rev. Mol. Cell Biol.* **11**, 633-643. doi:10.1038/nrm2957

Pasapera, A. M., Schneider, I. C., Rericha, E., Schlaepfer, D. D. and Waterman, C. M. (2010). Myosin II activity regulates vinculin recruitment to focal adhesions through FAK-mediated paxillin phosphorylation. *J. Cell Biol.* **188**, 877-890. doi:10.1083/jcb.200906012

Pedrotty, D. M., Klinger, R. Y., Badie, N., Hinds, S., Kardashian, A. and Bursac, N. (2008). Structural coupling of cardiomyocytes and noncardiomyocytes: quantitative comparisons using a novel micropatterned cell pair assay. *Am. J. Physiol. Heart Circ. Physiol.* **295**, H390-H400. doi:10.1152/ajpheart.91531.2007

Peter, A. K., Bjerke, M. A. and Leinwand, L. A. (2016). Biology of the cardiac myocyte in heart disease. *Mol. Biol. Cell* **27**, 2149-2160. doi:10.1091/mbc.E16-01-0038

Ponce-Balbuena, D., Guerrero-Serna, G., Valdivia, C. R., Caballero, R., Diez-Guerra, F. J., Jiménez-Vázquez, E. N., Ramírez, R. J., Monteiro da Rocha, A., Herron, T. J., Campbell, K. F. et al. (2018). Cardiac Kir2.1 and NaV1.5 channels traffic together to the sarcolemma to control excitability. *Circ. Res.* **122**, 1501-1516. doi:10.1161/CIRCRESAHA.117.311872

Ross, R. S. and Borg, T. K. (2001). Integrins and the myocardium. *Circ. Res.* **88**, 1112-1119. doi:10.1161/hh1101.091862

Rothenberg, K. E., Neibart, S. S., Lacroix, A. S. and Hoffman, B. D. (2015). Controlling cell geometry affects the spatial distribution of load across vinculin. *Cell. Mol. Bioeng.* **8**, 364-382. doi:10.1007/s12195-015-0404-9

Rothenberg, K. E., Scott, D. W., Christoforou, N. and Hoffman, B. D. (2018). Vinculin force-sensitive dynamics at focal adhesions enable effective directed cell migration. *Biophys. J.* **114**, 1680-1694. doi:10.1016/j.bpj.2018.02.019

Samarel, A. M. (2005). Costameres, focal adhesions, and cardiomyocyte mechanotransduction. *Am. J. Physiol. Heart Circ. Physiol.* **289**, H2291-H2301. doi:10.1152/ajpheart.00749.2005

Sampson, L. J., Leyland, M. L. and Dart, C. (2003). Direct interaction between the actin-binding protein filamin-A and the inwardly rectifying potassium channel, Kir2.1. *J. Biol. Chem.* **278**, 41988-41997. doi:10.1074/jbc.M307479200

Schoenwaelder, S. M. and Burridge, K. (1999). Bidirectional signaling between the cytoskeleton and integrins. *Curr. Opin. Cell Biol.* **11**, 274-286. doi:10.1016/S0955-0674(99)80037-4

Schumacher, S. M. and Martens, J. R. (2010). Ion channel trafficking: a new therapeutic horizon for atrial fibrillation. *Heart Rhythm* **7**, 1309-1315. doi:10.1016/j.hrthm.2010.02.017

Slack-Davis, J. K., Martin, K. H., Tilghman, R. W., Iwanicki, M., Ung, E. J., Autry, C., Luzzio, M. J., Cooper, B., Kath, J. C., Roberts, W. G. et al. (2007). Cellular characterization of a novel focal adhesion kinase inhibitor. *J. Biol. Chem.* **282**, 14845-14852. doi:10.1074/jbc.M606695200

Stockklausner, C., Ludwig, J., Ruppersberg, J. P. and Klöcker, N. (2001). A sequence motif responsible for ER export and surface expression of Kir2.0 inward rectifier K+ channels. *FEBS Lett.* **493**, 129-133. doi:10.1016/S0014-5793(01)02286-4

Thery, M., Racine, V., Piel, M., Pepin, A., Dimitrov, A., Chen, Y., Sibarita, J.-B. and Bornens, M. (2006). Anisotropy of cell adhesive microenvironment governs cell internal organization and orientation of polarity. *Proc. Natl. Acad. Sci. USA* **103**, 19771-19776. doi:10.1073/pnas.0609267103

Utrilla, R. G., Nieto-Marín, P., Alfayate, S., Tinaquero, D., Matamoros, M., Pérez-Hernández, M., Sacristán, S., Ondo, L., de Andrés, R., Díez-Guerra, F. J. et al. (2017). Kir2.1-Nav1.5 channel complexes are differently regulated than Kir2.1 and Nav1.5 channels alone. *Front. Physiol.* **8**, 903. doi:10.3389/fphys.2017.00903

Vaidyanathan, R., Taffet, S. M., Vikstrom, K. L. and Anumonwo, J. M. B. (2010). Regulation of cardiac inward rectifier potassium current (I(K1)) by synapse-associated protein-97. *J. Biol. Chem.* **285**, 28000-28009. doi:10.1074/jbc.M110.110858

Vaidyanathan, R., Vega, A. L., Song, C., Zhou, Q., Tan, B. H., Berger, S., Makielski, J. C. and Eckhardt, L. L. (2013). The interaction of caveolin 3 protein with the potassium inward rectifier channel Kir2.1: physiology and pathology related to long qt syndrome 9 (LQT9). *J. Biol. Chem.* **288**, 17472-17480. doi:10.1074/jbc.M112.435370

Varkevisser, R., Houtman, M. J., Waasdorp, M., Man, J. C., Heukers, R., Takanari, H., Tieland, R. G., Van Bergen En Henegouwen, P. M., Vos, M. A. and van der Heyden, M. A. G. (2013). Inhibiting the clathrin-mediated endocytosis pathway rescues K(IR)2.1 downregulation by pentamidine. *Pflugers Arch.* **465**, 247-259. doi:10.1007/s00424-012-1189-5

Vega, A. L., Tester, D. J., Ackerman, M. J. and Makielski, J. C. (2009). Protein kinase A-dependent biophysical phenotype for V227F-KCNJ2 mutation in catecholaminergic polymorphic ventricular tachycardia. *Circ. Arrhythm Electrophysiol.* **2**, 540-547. doi:10.1161/CIRCEP.109.872309

Wahler, G. M. (1992). Developmental increases in the inwardly rectifying potassium current of rat ventricular myocytes. *Am. J. Physiol.* **262**, C1266-C1272. doi:10.1152/ajpcell.1992.262.5.C1266

Wang, Y., Cao, H., Chen, J. and McNiven, M. A. (2011). A direct interaction between the large GTPase dynamin-2 and FAK regulates focal adhesion dynamics in response to active Src. *Mol. Biol. Cell* **22**, 1529-1538. doi:10.1091/mbc.e10-09-0785

Wischmeyer, E., Döring, F. and Karschin, A. (1998). Acute suppression of inwardly rectifying Kir2.1 channels by direct tyrosine kinase phosphorylation. *J. Biol. Chem.* **273**, 34063-34068. doi:10.1074/jbc.273.51.34063

Wozniak, M. A., Modzelewska, K., Kwong, L. and Keely, P. J. (2004). Focal adhesion regulation of cell behavior. *Biochim. Biophys. Acta* **1692**, 103-119. doi:10.1016/j.bbamcr.2004.04.007

Zamir, E., Katz, B. Z., Aota, S., Yamada, K. M., Geiger, B. and Kam, Z. (1999). Molecular diversity of cell-matrix adhesions. *J. Cell Sci.* **112**, 1655-1669.

Zaritsky, J. J., Eckman, D. M., Wellman, G. C., Nelson, M. T. and Schwarz, T. L. (2000). Targeted disruption of Kir2.1 and Kir2.2 genes reveals the essential role of the inwardly rectifying K(+) current in K(+)-mediated vasodilation. *Circ. Res.* **87**, 160-166. doi:10.1161/01.RES.87.2.160

Zhan, Y., Tremblay, M. R., Melian, N. and Carbonetto, S. (2005). Evidence that dystroglycan is associated with dynamin and regulates endocytosis. *J. Biol. Chem.* **280**, 18015-18024. doi:10.1074/jbc.M409682200